Journal of Marine Science and Application (2026) 25: 1424-1445
https://doi.org/10.1007/s11804-025-00774-6

RESEARCH ARTICLE

Observer-Based Distributed Prescribed-Time Containment Control for Multiple Underactuated Unmanned Surface Vehicles with Input Saturation and Full-State Constraints

Yuheng Song[1,2], Linsen Feng[1,2], Yanchao Sun[1,2], Zhongchao Deng[1,2] and Hongde Qin[1,2]

Received: 06 April 2025 / Accepted: 31 July 2025
© Harbin Engineering University and Springer-Verlag GmbH Germany, part of Springer Nature 2026

Abstract

This study solves the problem of distributed prescribed-time containment control of underactuated unmanned surface vehicles (USVs) in the presence of parametric uncertainties, unmodeled dynamics, and external environmental disturbances. Under the leader-follower approach, considering that only a subset of followers has access to the trajectory information of the virtual leaders, a novel distributed adaptive prescribed-time observer is presented. Given the general uncertainties in the USV model, an improved prescribed-time extended state observer (PTESO) is established for estimation and compensation. Then, a prescribed-time command filter and a filter compensation system are introduced to estimate the virtual control signal and address the differential explosion problem. Furthermore, a prescribed-time anti-saturation auxiliary system is proposed to address the actuator input saturation. Moreover, a prescribed-time distributed guidance protocol and a distributed control protocol are developed for each USV by employing the backstepping method and the variable transformation strategy. The use of graph theory, prescribed-time theory, and Lyapunov analysis ensures that the follower converges to the convex hull spanned by the multiple virtual leaders within a prescribed time. This approach involves dynamically adjusting the distance among USVs according to the channel width. The errors associated with the distributed adaptive observer and PTESO exhibit bounded convergence within a prescribed time. In addition, the full-state constraints have been confirmed, which implies that the containment errors, including position, velocity, and acceleration errors of the followers, can converge and remain bounded within a prescribed time. The originality of this study lies in overcoming key challenges, including general model uncertainties, actuator saturation, limited information available to follower USVs, and ensuring prescribed-time convergence. Future research can explore an event-based communication protocol to realize intermittent communication among USVs.

Keywords Unmanned surface vehicles; Prescribed time; Distributed adaptive observer; Extended state observer; Input saturation; Full-state constraints

Article Highlights

- A prescribed-time distributed control law for unmanned surface vehicles (USVs) based on a new prescribed-time distributed adaptive observer is proposed.
- A prescribed-time extended state observer is constructed for compensation to address model uncertainty, and a prescribed-time anti-saturation auxiliary system is designed to avoid actuator input saturation.
- This research focuses on overcoming key challenges associated with general model uncertainties, actuator saturation, constrained information availability for USVs, and guaranteeing prescribed-time convergence.

✉ Yanchao Sun
sunyanchao@hrbeu.edu.cn

[1] College of Shipbuilding Engineering, Harbin Engineering University, Harbin 150001, China

[2] National Key Laboratory of Autonomous Marine Vehicle Technology, Harbin Engineering University, Harbin 150001, China

1 Introduction

Given the increasing complexity of maritime missions, single unmanned surface vehicles (USVs), which are limited by their single type of equipment, constrained resources, and insufficient energy capacity, make them inadequate for contemporary mission requirements (Gu et al., 2022; Li et al., 2022; Mu et al., 2022). Zhang et al. (2018) developed a virtual submerged floating operational system to simulate underwater intervention tasks for reducing underwater operation costs and risks. Jiang et al. (2025) proposed an autonomous operation framework for UVMS to enable complex underwater interventions such as valve switching and pipe handling. The adoption of cooperative strategies among multiple USVs, which form a multi-agent system (MAS), not only broadens their environmental perception but also extends their operational reach and enhances time efficiency through parallel operations (Li et al., 2021). Such coordinated operations are extensively utilized in various

applications, including environmental monitoring, aquatic data collection, search and rescue missions, and military mine detection (Jiang et al., 2021; Zhang et al., 2021).

The cooperative control of MASs is primarily facilitated through distributed control mechanisms (Peng et al., 2021). In distributed control, agents exchange information through a communication network and calculate their control inputs based on their own and their neighbors' information. Wu et al. (2023) investigated the finite-time output feedback control for multiple USVs considering velocity and input constraints. In Chen et al. (2023), a fixed-time tracking consensus and containment control of second-order MASs is constructed using the nonsingular sliding-mode method. In these studies, the combination of the leader-follower approach and topology graph theory has shown significant advantages, resulting in a more concise design for the control algorithm and a more flexible formation configuration. However, in distributed leader-follower control, only a subset of the followers can receive information from the leader. Guaranteeing that the remaining followers also receive the information of the leader remains an urgent concern to be solved. In a previous study (Chen and Shan, 2021), a nonlinear distributed observer was designed for each follower to estimate the state of the leader. It guaranteed that the observation errors converged to a bounded region within a finite time. Similarly, when evaluating distributed containment control in a directed topology, Gao et al. (2022) proposed a distributed fixed-time observer to estimate the states of the leader spacecraft. Although these methods can accurately obtain the states of the leader, most of them require the design of complex observers, and the convergence of observation errors still remains within a finite or fixed time. Therefore, guaranteeing the convergence time of observational errors of the distributed observers within a predefined time continues to be a key challenge.

The dynamics equation of USVs generally contains parametric uncertainties, unmodeled dynamics, and external disturbances. These factors together compose the general uncertainties. In practical applications, input saturation is a common problem due to the physical constraints of the actuators. These challenges significantly affect the tracking performance of USVs, especially in the case of distributed containment control. To overcome these concerns, Zhang et al. (2020) explored the precise trajectory tracking control of USVs under external disturbances. A fixed-time disturbance observer was employed to identify external disturbances. Li et al. (2024) established a robust practical prescribed-time control scheme to address the trajectory tracking problem of USVs under input saturation and unknown disturbances. Li et al. (2020) solved the trajectory tracking control problem encountered by autonomous underwater vehicles (AUVs) under parameter uncertainties and external disturbances. They designed a data-driven method to optimize the linear extended state observer (ESO). Wang et al. (2025) introduced a position acoustic vision servo control system based on deep reinforcement learning (DRL) to address the precise docking problem of AUVs under the limited field of view of sonar imaging. Furthermore, Wu et al. (2022) examined the path tracking control problem of underactuated USVs in a wireless network environment. Moreover, an ESO was employed in local loops to estimate unknown uncertainties caused by unmodeled dynamics and environmental disturbances. Although existing studies have established corresponding methods, accurately estimating general uncertainties within a prescribed time remains difficult (Liu et al., 2020; Zhang et al., 2019). To overcome this difficulty, Li et al. (2023) addressed the trajectory tracking control of AUVs and introduced a prescribed-time disturbance observer to guarantee that the convergence time of the observation error remains independent of the initial conditions. In addition, the prescribed-time extended state observer (PTESO) proposed in Cui and Jin (2021) can effectively estimate disturbances within a specified time predefined by humans.

In the design of containment controllers for USVs, the robustness against general uncertainties in the control algorithm needs to be considered. The convergence speed of the tracking errors is also a key indicator. Although many works have attempted to achieve fixed-time convergence, this method still has notable limitations. Specifically, fixed-time control approaches frequently require the setting of a large number of parameters to achieve the desired settling time, which can be inconvenient for practical applications. Furthermore, the estimated convergence time is relatively conservative. To overcome this problem, Song et al. (2017) proposed the prescribed-time control method, which allows the system to stabilize within a prescribed time and only depends on a single time parameter. This approach significantly simplifies the design of controller parameters and results in the explicit estimation of the convergence time. For example, Liu et al. (2021) developed an adaptive fuzzy prescribed-time containment control approach. The aim was to guarantee that all followers reached the convex hull defined by the leader within a prescribed time. Wang et al. (2021) investigated the problem of prescribed-time regulation for cascaded systems incorporating integral forms and control input constraints. The application of prescribed-time cascaded stability enabled the separate design of the controller and governor. However, existing studies mainly focus on containment errors in position or attitude. This method often neglects errors in velocity and acceleration. When the constraints of these errors are considered, the system guarantees improved robustness and global convergence capabilities (Ye and Song, 2023).

This study tackles the distributed containment control of underactuated USVs in the presence of general uncertainties and input saturation. Specifically, a distributed pre-

scribed-time containment control approach under an undirected communication topology is utilized. The novelties and contributions of our work are provided as follows.

1) To guarantee that the remaining followers can obtain the desired trajectory formed by the convex hull spanned by multiple virtual leaders, this study introduces a distributed adaptive observer with a prescribed-time control, which is improved using a distributed observer. Within this framework, a predefined scalar function is integrated into the observer and cooperates with a prescribed-time adaptive law. By choosing appropriate parameters, the observation errors can converge to a small neighborhood around the origin within a prescribed time. Notably, the results differ from the failure of the observer to achieve convergence within the prescribed time in Chen and Shan (2021), as well as with the fixed-time convergence results in Gao et al. (2022).

2) ESO was used to estimate general uncertainties in studies by Li et al. (2020) and Wu et al. (2022), which is unrealistic in the control of USVs due to the difficulty of parameter adaptation to complex external disturbances. In response to the general uncertainties in the model, the present study enhances the PTESO by avoiding the requirements of obtaining prior knowledge regarding the upper bound of the disturbance and using an additional Levant's differentiator. Adjusting the observer coefficients and time of the scalar function guarantees that the observation errors of velocity and general uncertainties converge and remain bounded within a prescribed time.

3) To avoid using the differential signal of the virtual control signal in the control protocol, a new prescribed-time command filter (PTCF) is designed based on the NLTD. The differential operation of the guidance signal is effectively avoided, which addresses the problem of "differential explosion" and reduces the burden of computational resources for USVs. Unlike the methods of Yi et al. (2017) and Gu et al. (2019), which can only achieve finite-time convergence, the PTCF can achieve prescribed-time convergence and explicitly estimate the convergence time. Meanwhile, a prescribed-time filter compensation system is constructed to address the filter error.

4) Apart from ensuring the prescribed-time bounded convergence of containment errors, this method also accounts for actuator input saturation issues. The auxiliary system is integrated with the prescribed-time scaling function. By adopting the backstepping method and the variable transformation strategy, a prescribed-time distributed guidance protocol and a distributed control protocol are established for each USV. The full-state containment errors can converge and be bounded within a prescribed time. Therefore, the proposed approach implements full-state constraints and enhances system robustness against disturbances and uncertainties compared with the methods of Liu et al. (2021), Wang et al. (2021), and Ye and Song (2023).

The remainder of the paper is organized as follows. The notation, graph theory, and problem description are discussed in Section 2. A prescribed-time distributed guidance protocol and a distributed control protocol are developed in Section 3. To test the effectiveness of our proposed methods, numerical simulations are conducted in Section 4. Section 5 elaborates the main conclusions.

2 Preliminaries and problem formulation

2.1 Notation

The basic mathematical symbols and definitions of this research are displayed in Table 1.

Table 1 Symbols and definitions

Symbols	Definitions
$\boldsymbol{R}^{M\times N}$	Set of $M \times N$ real matrices
$\mathbf{0}_{M\times N}$	Zero matrix of $M \times N$
$\mathbf{1}_N$	Column vector of $N \times 1$
$\boldsymbol{I}_N$	Identity matrix of $N \times N$
$\|\cdot\|_2$	Frobenius norm of a vector
$\mathrm{sign}(\cdot)$	Signum function
$\lambda_{\min}$	Min-eigenvalues of a matrix
$\lambda_{\max}$	Max-eigenvalues of a matrix
$\otimes$	Kronecker product
$\lvert\boldsymbol{x}\rvert$	Absolute value of a vector
$x^{(k)}$	k-th derivative of x
(x, y)	Inner product operation
$\mathrm{sat}(\cdot)$	Saturation function

2.2 Communication graph

In this research, the algebraic graph theory is used to characterize the communication topology structure between the leaders and followers in the USV system, as well as the intercommunication relationships among the followers. A topology graph $\mathcal{G}=(\mathcal{V},\mathcal{E},\mathcal{A})$ composed of a set of nodes $\mathcal{V}=\{v_1,v_2,\cdots,v_{M+N}\}$ and a set of edges $\mathcal{E}\subseteq v_i\times v_j$ is considered to represent this system. In the system, the nodes denote the USVs, and the edges signify the communication links among them. In the given topological graph, each node v_i represents a USV, while the edge set $\mathcal{E}$ describes the communication links among adjacent USV nodes. For directed graphs, an edge $(v_i, v_j)\in\mathcal{E}$ suggests that the node v_i can receive information from node v_j. In this case, node v_j is referred to as the parent node of node v_i, and node v_i is the child node of node v_j. The set of all parent nodes of node v_i is denoted as N_i, which is called the neighborhood set of the node v_i. Mean-

while, in an undirected communication topology, adjacent nodes can communicate with each other, which is represented by the set $(v_i, v_j) \in \mathcal{E} \Leftrightarrow (v_j, v_i) \in \mathcal{E}$.

In the communication topology graph G, a continuous communication link from node v_j to node v_i can be represented by various connected edges, which are denoted as $\{(v_i, v_k), (v_k, v_l), \cdots, (v_l, v_j)\}$. A subgraph $\bar{\mathcal{G}}$ is assumed to exist within the graph G, which can reach all other nodes via continuous communication links starting from a root node v_0. In this case, the subgraph $\bar{\mathcal{G}}$ has a spanning tree rooted at v_0, and the topology graph G possesses a spanning tree.

Specific matrices can be used to describe the structural attributes of a communication topology graph. The adjacency matrix for the followers is defined as $\bar{\boldsymbol{\mathcal{A}}} = [a_{ij}] \in \boldsymbol{R}^{M \times M}$, where the matrix element is $a_{ij} = 1$ if condition $(v_i, v_j) \in \mathcal{E}$ is satisfied, and $a_{ij} = 0$ otherwise. Typically, it is assumed that the diagonal elements $a_{ii} = 0$, indicating that a node does not connect to itself. When a leader is present in the system, an adjacency matrix for the leader can be defined as $\bar{\boldsymbol{\mathcal{A}}}_{N+1} = \text{diag}\{a_{1(N+1)}, \cdots, a_{M(N+1)}\} \in \boldsymbol{R}^{M \times M}$, where the matrix element $a_{i(N+1)} = 1$ if $(\boldsymbol{v}_i, \boldsymbol{v}_{N+1}) \in \mathcal{E}$, and $a_{i(N+1)} = 0$ otherwise.

When M followers and N leaders are present in the system, $\mathcal{V}_F = \{v_1, v_2, \cdots, v_M\}$ and $\mathcal{V}_L = \{v_{M+1}, \cdots, v_{M+N}\}$, respectively, defines the sets of follower and leader nodes. Then, the adjacency matrix of the entire communication topology graph G can be represented as $\boldsymbol{\mathcal{A}} = [a_{ij}] \in \boldsymbol{R}^{(M+N)\times(M+N)}$, and the in-degree Laplacian matrix of the entire communication topology graph G can be defined as $\boldsymbol{D} = \text{diag}\{b_1, \cdots, b_{M+N}\} \in \boldsymbol{R}^{(M+N)\times(M+N)}$, where $b_i = \sum_{j=1}^{M+N} a_{ij}$. Under this context, the Laplacian matrix of the entire distributed system can be denoted as $\boldsymbol{L} = \boldsymbol{D} - \boldsymbol{A} \in \boldsymbol{R}^{(M+N)\times(M+N)}$. Furthermore, no information transfer from followers to leaders and among the leaders is assumed. Under this assumption, the Laplacian matrix can be expressed as the following block matrix:

$$\boldsymbol{L} = \begin{bmatrix} \boldsymbol{L}_1 & \boldsymbol{L}_2 \\ \boldsymbol{0}_{N\times M} & \boldsymbol{0}_{N\times N} \end{bmatrix} \tag{1}$$

where $\boldsymbol{L}_1 \in \boldsymbol{R}^{M\times M}$ and $\boldsymbol{L}_2 \in \boldsymbol{R}^{M\times N}$.

2.3 Problem formulation

The leader is assumed to be a virtual leader, which is a pre-planned trajectory $\boldsymbol{\eta}_k(\theta_k) \in \boldsymbol{R}^2$, where $\theta_k = v_s t$ denotes the trajectory update variable and the parameter v_s signifies the update speed of the trajectory variable to be set. The followers are underactuated USVs, and their planar three-degree-of-freedom kinematics and dynamics differential equations are provided as follows (Fossen, 2011):

$$\begin{cases} \dot{\boldsymbol{\eta}}_i = \boldsymbol{R}_i(\psi_i)\boldsymbol{v}_i \\ \boldsymbol{M}_i\dot{\boldsymbol{v}}_i = \text{sat}(\boldsymbol{\tau}_i) - \boldsymbol{C}(\boldsymbol{v}_i)\boldsymbol{v}_i - \boldsymbol{D}(\boldsymbol{v}_i)\boldsymbol{v}_i + \boldsymbol{\tau}_{iw}(t) \end{cases} \tag{2}$$

where $\boldsymbol{\eta}_i = [x_i, y_i, \psi_i]^{\mathrm{T}}$ denotes the position (x_i, y_i) and heading angle ψ_i of the i-th USV in the earth-fixed frame $O_{\mathrm{E}}X_{\mathrm{E}}Y_{\mathrm{E}}$, as depicted in Figure 1, and $\boldsymbol{v}_i = [u_i, v_i, r_i]^{\mathrm{T}}$ signifies the surge velocity u_i, sway velocity v_i, and angular rate r_i in the body-fixed frame $O_{\mathrm{B}}X_{\mathrm{B}}Y_{\mathrm{B}}$. $\boldsymbol{M}_i \in \boldsymbol{R}^{3\times 3}$ refers to the mass-inertia matrix of the USV, which consists of the nominal mass-inertia matrix $\boldsymbol{M}_i^*$ and the additional mass matrix $\Delta\boldsymbol{M}_i$ induced by hydrodynamics. $\boldsymbol{C}(\boldsymbol{v}_i) \in \boldsymbol{R}^{3\times 3}$ is the Coriolis/centrifugal matrix, $\boldsymbol{D}(\boldsymbol{v}_i) \in \boldsymbol{R}^{3\times 3}$ denotes the nonlinear damping matrix, and $\boldsymbol{\tau}_{iw}(t) \in \boldsymbol{R}^3$ signifies unknown time-varying disturbance forces resulting from external factors such as wind, waves, and currents. $\boldsymbol{R}_i(\psi_i) \in \boldsymbol{R}^{3\times 3}$ is the rotation matrix for transforming from the body-fixed frame to the earth-fixed frame, which satisfies the condition $\dot{\boldsymbol{R}}_i^{\mathrm{T}}(\psi_i) = -r_i\boldsymbol{S}\boldsymbol{R}_i^{\mathrm{T}}(\psi_i)$. Thus, we have

$$\boldsymbol{R}_i(\psi_i) = \begin{bmatrix} \cos\psi_i & -\sin\psi_i & 0 \\ \sin\psi_i & \cos\psi_i & 0 \\ 0 & 0 & 1 \end{bmatrix}, \boldsymbol{S} = \begin{bmatrix} 0 & -1 & 0 \\ 1 & 0 & 0 \\ 0 & 0 & 0 \end{bmatrix} \tag{3}$$

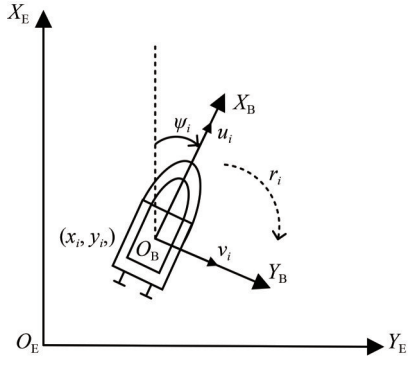


Figure 1 Reference frame

When input saturation is considered, the actual control input of the USV is denoted as $\text{sat}(\boldsymbol{\tau}_i)$. $\boldsymbol{\tau}_i = [\tau_{iu}, 0, \tau_{ir}] \in \boldsymbol{R}^3$ denotes the desired control input for the USV, while τ_{iu} and τ_{ir} refer to thrust and torque, respectively. $\Delta\boldsymbol{\tau}_i = \text{sat}(\boldsymbol{\tau}_i) - \boldsymbol{\tau}_i$ signifies the difference between $\text{sat}(\boldsymbol{\tau}_i)$ and $\boldsymbol{\tau}_i$. $\text{sat}(\boldsymbol{\tau}_i)$ can be specifically expressed as

$$\text{sat}(\boldsymbol{\tau}_i) = \begin{cases} u_{im}, & \tau_i > u_{im} \\ \tau_i, & -u_{im} < \tau_i < u_{im} \\ -u_{im}, & \tau_i < -u_{im} \end{cases} \tag{4}$$

where u_{im} represents the maximum allowable control input for the USVs. In this study, $u_{im} = 50$ N (N·m).

Moreover, if $\Delta\boldsymbol{M}_i$, $\boldsymbol{C}(\boldsymbol{v}_i)$, $\boldsymbol{D}(\boldsymbol{v}_i)$, and $\boldsymbol{\tau}_{iw}(t)$ are unknown, then the dynamics equation of the USV can be transformed as follows:

$$\dot{\boldsymbol{v}}_i = \boldsymbol{M}_i^{*-1}\boldsymbol{\tau}_i + \boldsymbol{f}_i - \boldsymbol{M}_i^{*-1}\Delta\tau_i \tag{5}$$

where $\boldsymbol{f}_i = \boldsymbol{M}_i^{*-1}\left(-\boldsymbol{\Delta}\boldsymbol{M}_i\dot{\boldsymbol{v}} - C(\boldsymbol{v}_i)\boldsymbol{v}_i - \boldsymbol{D}(\boldsymbol{v}_i)\boldsymbol{v}_i + \boldsymbol{\tau}_{iw}(t)\right)$ is the general uncertainties term composed of parametric uncertainties, unmodeled dynamics, and external environmental disturbances.

Definition 1 A subset $\boldsymbol{X}$ is considered within the real vector space $\boldsymbol{S} \in \boldsymbol{R}^n$, and $C_o(\boldsymbol{X})$ represents the convex hull formed by all points in set $\boldsymbol{X} = \{x_1, x_2, \cdots, x_n\} \in \boldsymbol{R}^n$, that is,

$$C_o(\boldsymbol{X}) = \left\{ \sum_{i=1}^{n} a_i x_i \middle| x_i \in \boldsymbol{X}, \sum_{i=1}^{n} a_i = 1 \right\} \tag{6}$$

Similar to the works of Gu et al. (2019) and Ye and Song (2023), this study aims to design a distributed control protocol based on a prescribed-time approach. The objective is to guarantee that the containment errors converge to a small neighborhood of the origin after a prescribed time. Moreover, the full states of the containment errors of the followers converge rapidly to the origin within a prescribed time, that is,

$$\forall t \geqslant T_1, \left\| \boldsymbol{\eta}_i - \sum_{k=M+1}^{M+N} \lambda_k \boldsymbol{\eta}_k(\theta_k) \right\| \leqslant l, i = 1, \cdots, M \tag{7}$$

$$\lim_{t \to T_3^-} \left\| \boldsymbol{\eta}_i^{(j)} - \sum_{k=M+1}^{M+N} \lambda_k \boldsymbol{\eta}_k{}^{(j)}(\theta_k) \right\| = 0, i = 1, \cdots, M;\ j = 0, \cdots, q \tag{8}$$

where $\sum_{k=M+1}^{M+N} \lambda_k = 1$, l is a small positive constant.

2.4 Assumptions and Lemmas

Assumption 1 The communication topology G of the distributed USV system comprises at least one spanning tree, with the virtual leader acting as the root node. In addition, the subgraph $\bar{\mathcal{G}}$ among the USVs (excluding the root node) is an undirected graph.

Lemma 1 (Mei et al., 2012) Under the condition of Assumption 1, the matrix $\boldsymbol{L}_1$ is proven to be symmetric and positive definite. Furthermore, every element within matrix $-\boldsymbol{L}_1^{-1}\boldsymbol{L}_2$ is non-negative, and each row of the matrix meets the constraint that the sum of its elements equals 1, which is denoted as $-\boldsymbol{L}_1^{-1}\boldsymbol{L}_2\boldsymbol{1}_N = \boldsymbol{1}_M$.

Assumption 2 The trajectories of each virtual leader are continuously smooth. That is, the parameterized trajectory $\boldsymbol{\eta}_k(\theta_k)$ of the virtual leader, its first-order derivative v_k, and its second-order derivative a_k are bounded. Specifically, the derivatives of the acceleration a_k are assumed to be known and bounded, which means that the Euclidean norm for the derivative of the acceleration of the trajectory is bounded, that is, $\left\| \left(\dot{\bar{a}}_{kx}, \dot{\bar{a}}_{ky} \right) \right\|_2 \leqslant \gamma_k$.

Assumption 3 (Sun et al. 2024) The Euclidean norm for the derivative of the term of general uncertainties f concerning time t in the dynamics model of the USV is bounded, which satisfies the condition $\left\| \dot{f}_i \right\|_2 < \boldsymbol{\Delta}$.

Assumption 4 (Li et al. 2023) The Euclidean norm of the difference $\Delta\bar{\tau}_i$ between the actual and estimated input for the USVs is bounded, which satisfies the condition $\left\| \Delta\bar{\tau}_i \right\|_2 < \Lambda$.

Remark 1 A few assumptions have been made to stipulate the research content and facilitate the controller design. These assumptions are typically used in research on USVs or AUVs. Compared with large ships, USVs are exposed to more stable wind, waves, and ocean currents, that is, $\left\| \dot{f}_i \right\|_2 < \boldsymbol{\Delta}$. Given that the input power of the USVs is limited by electrical energy, the thrust of the thrusters is bounded. Meanwhile, the saturation difference $\Delta\bar{\tau}_i$ is assumed to have an upper bound. Therefore, the assumptions are all reasonable.

Definition 2 Building upon the foundation of the definition in Ye and Song (2023), a user-defined prescribed-time constant T_x is introduced. A function is referred to as a prescribed-time scaling function when it satisfies the following conditions.

1) When $t \in [0, T_x)$, $\mu(t)$ satisfies $\mu(0) = 1$ and $\mu(T_x) = +\infty$, which belong to a class of positive-definite and non-decreasing continuous functions.

2) When $t \in [0, T_x)$, $\dot{\mu}/\mu^2$ is a bounded continuous function.

3) When $t \in [0, T_x)$, $\mu(t)$ possesses ∞ continuous derivatives.

4) When $t \in [T_x, +\infty)$, $\mu(t)$ is a positive-definite continuous bounded function.

A function that satisfies the abovementioned conditions is given as follows:

$$\mu(t) = \begin{cases} \left(\dfrac{T_x}{T_x - t} \right)^{m+n}, & t < T_x \\ c, & t \geqslant T_x \end{cases} \tag{9}$$

where n is the order of the controlled system. The parameters m and c are the positive integers used in the design.

Lemma 2 (Ye and Song, 2023) Considering a prescribed-time scaling function $\mu(t)$, a Lyapunov function $V(t): [0, T_x) \to [0, +\infty)$ satisfying the following inequality is assumed:

$$\dot{V}(t) \leqslant -2k\mu(t)V(t) + \mu(t)\Gamma(t) \tag{10}$$

where k is a positive constant, and $\Gamma(t)$ is an unknown time-varying bounded disturbance. Then, $V(t)$ will converge within a bounded range within the prescribed time T_x.

Lemma 3 (Slotine and Li, 1991) If the eigenvalues of

the coefficient matrix $\boldsymbol{A}$ of a linear deterministic system $\dot{\boldsymbol{x}} = \boldsymbol{A}\boldsymbol{x}$ all have negative real parts, then any symmetric positive-definite matrix $\boldsymbol{Q}$ has a symmetric positive-definite matrix $\boldsymbol{P}$, which satisfies

$$\boldsymbol{A}^{\mathrm{T}}\boldsymbol{P} + \boldsymbol{P}^{\mathrm{T}}\boldsymbol{A} = -\boldsymbol{Q} \tag{11}$$

Definition 3 (Zhang, et al., 2021) A real symmetric matrix $\boldsymbol{Q}$ is said to be positive definite if, for all non-zero vectors $\boldsymbol{x}$, the quadratic form satisfies $\boldsymbol{x}^{\mathrm{T}}\boldsymbol{Q}\boldsymbol{x} > 0$. Equivalently, $\boldsymbol{Q}$ is positive definite if all its eigenvalues are strictly positive.

3 Control protocol design based on prescribed-time distributed observer

In this section, our design objective is to develop a distributed containment control protocol for underactuated USVs. First, the states of the virtual leader are assumed to be only accessible to the USVs on either side of the formation. To guarantee that other followers can track along the convex hull formed by the two virtual leaders, a prescribed-time distributed adaptive observer is designed for each follower. Second, a PTESO is modified based on the nominal dynamic model of USVs. The PTESO estimates the general uncertainty terms present in the USV model within a prescribed time using its own position and heading information. Then, a PTCF and a filter compensation system are designed to estimate the virtual guidance protocol. Subsequently, employing the backstepping method and the variable substitution strategy, the prescribed-time distributed guidance and control protocols are designed for each USV. This design allows each USV to pass through the channel equidistantly in formation and adaptively adjust the distances among them based on the channel width, as illustrated in Figure 2. Subsequently, a stability analysis of the convergence of the distributed control protocol is conducted in the presence of model uncertainty and external disturbances. The block diagram of the control system is shown in Figure 3.

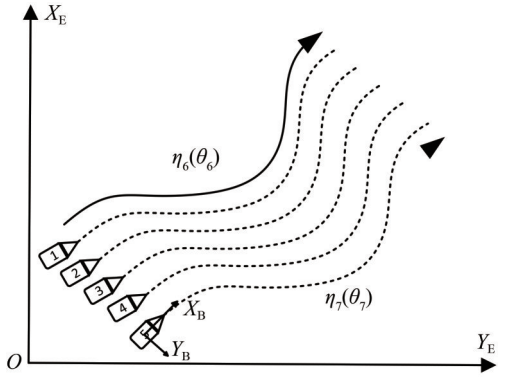


Figure 2 Passing through narrow channels

3.1 Prescribed-time distributed adaptive observer

A prescribed-time distributed adaptive observer is designed to acquire the desired trajectory information for each follower for estimating the convex hull spanned by the virtual leaders.

$$\begin{cases} \dot{\hat{\boldsymbol{\eta}}}_i = -k_1\mu_1(t)\tilde{\boldsymbol{\eta}}_i + \hat{\boldsymbol{v}}_i \\ \dot{\hat{\boldsymbol{v}}}_i = -k_2\mu_1(t)\tilde{\boldsymbol{v}}_i + \hat{\boldsymbol{a}}_i \\ \dot{\hat{\boldsymbol{a}}}_i = -k_3\mu_1(t)\tilde{\boldsymbol{a}}_i - \hat{\gamma}_i \mathrm{sign}(\tilde{\boldsymbol{a}}_i) \\ \dot{\hat{\gamma}}_i = \left\| \tilde{\boldsymbol{a}}_i \right\|_2 - \mu_1(t)\hat{\gamma}_i \end{cases}, i = 1, \cdots, M \tag{12}$$

where variables $\hat{\boldsymbol{\eta}}_i \in \boldsymbol{R}^{2*1}$, $\hat{\boldsymbol{v}}_i \in \boldsymbol{R}^{2*1}$, and $\hat{\boldsymbol{a}}_i \in \boldsymbol{R}^{2*1}$ represent the observed variables of position, velocity, and acceleration of the i-th follower concerning the convex hull formed by the virtual leaders, respectively. $\hat{\gamma}_i \in \boldsymbol{R}$ is the adaptive variable of the i-th follower, which is used to estimate an upper bound $\gamma_i \in \boldsymbol{R}$ on the norm of the accelera-

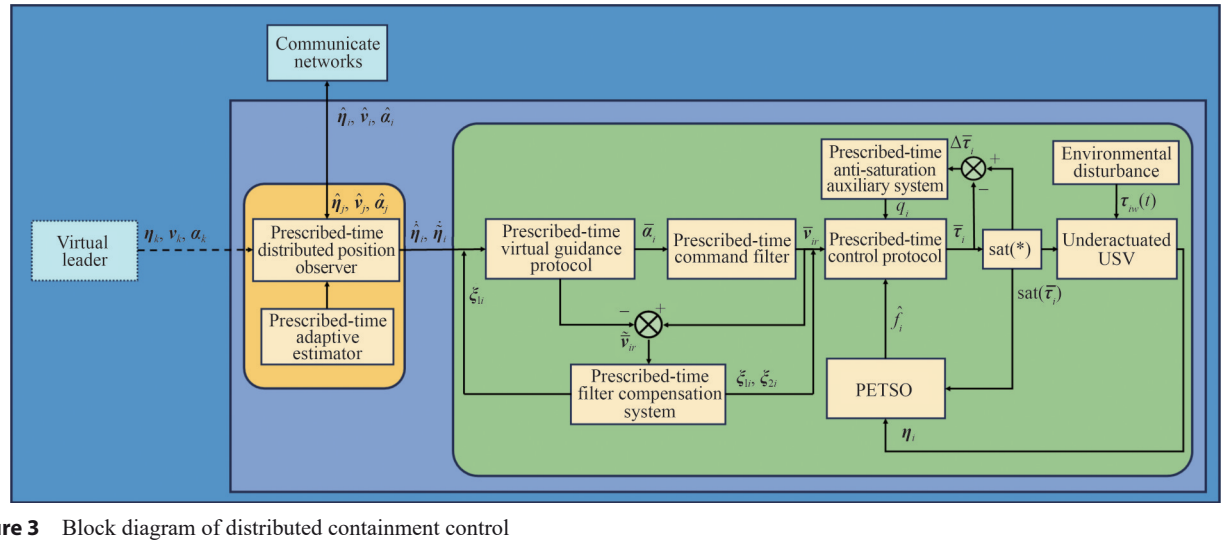


Figure 3 Block diagram of distributed containment control

tion derivative of the virtual leader.

The observation and adaptive estimation errors for each follower can be expressed as follows:

$$\begin{cases} \tilde{\boldsymbol{\eta}}_i = \sum\limits_{j\in N_i} \boldsymbol{a}_{ij}(\hat{\boldsymbol{\eta}}_i - \hat{\boldsymbol{\eta}}_j) + \sum\limits_{K=M+1}^{N} \boldsymbol{a}_{ik}(\hat{\boldsymbol{\eta}}_i - \boldsymbol{\eta}_k) \\ \tilde{\boldsymbol{v}}_i = \sum\limits_{j\in N_i} \boldsymbol{a}_{ij}(\hat{\boldsymbol{v}}_i - \hat{\boldsymbol{v}}_j) + \sum\limits_{K=M+1}^{N} \boldsymbol{a}_{ik}(\hat{\boldsymbol{v}}_i - \boldsymbol{v}_k) \\ \tilde{\boldsymbol{a}}_i = \sum\limits_{j\in N_i} \boldsymbol{a}_{ij}(\hat{\boldsymbol{a}}_i - \hat{\boldsymbol{a}}_j) + \sum\limits_{K=M+1}^{N} \boldsymbol{a}_{ik}(\hat{\boldsymbol{a}}_i - \boldsymbol{a}_k) \\ \tilde{\gamma}_i = \gamma_k - \hat{\gamma}_i \end{cases}, i = 1, \cdots, M \tag{13}$$

where variables $\boldsymbol{\eta}_k \in \boldsymbol{R}^{2*1}$, $\boldsymbol{v}_k \in \boldsymbol{R}^{2*1}$, and $\boldsymbol{a}_k \in \boldsymbol{R}^{2*1}$ represent the position, velocity, and acceleration of the leader k, respectively. Meanwhile, $\hat{\boldsymbol{\eta}}_j \in \boldsymbol{R}^{2*1}$, $\hat{\boldsymbol{v}}_j \in \boldsymbol{R}^{2*1}$, and $\hat{\boldsymbol{a}}_j \in \boldsymbol{R}^{2*1}$ are the observation variables of position, velocity, and acceleration of the j-th follower, respectively, concerning the convex hull spanned by the multiple virtual leaders. $\tilde{\gamma}_i \in \boldsymbol{R}$ denotes the adaptive estimation errors of the i-th follower.

To facilitate the proof of stability for the entire distributed adaptive observation errors, the observation errors of all USVs are consolidated into the following vector form:

$$\begin{cases} \tilde{\boldsymbol{\eta}} = (\boldsymbol{L}_1 \otimes \boldsymbol{I}_2)\hat{\boldsymbol{\eta}} + (\boldsymbol{L}_2 \otimes \boldsymbol{I}_2)\bar{\boldsymbol{\eta}}_k \\ \tilde{\boldsymbol{v}} = (\boldsymbol{L}_1 \otimes \boldsymbol{I}_2)\hat{\boldsymbol{v}} + (\boldsymbol{L}_2 \otimes \boldsymbol{I}_2)\bar{\boldsymbol{v}}_k \\ \tilde{\boldsymbol{a}} = (\boldsymbol{L}_1 \otimes \boldsymbol{I}_2)\hat{\boldsymbol{a}} + (\boldsymbol{L}_2 \otimes \boldsymbol{I}_2)\bar{\boldsymbol{a}}_k \\ \tilde{\gamma} = \gamma - \hat{\gamma} \end{cases} \tag{14}$$

where $\hat{\boldsymbol{\eta}} = \left[\hat{\boldsymbol{\eta}}_1^{\mathrm{T}}, \cdots, \hat{\boldsymbol{\eta}}_M^{\mathrm{T}}\right]^{\mathrm{T}} \in \boldsymbol{R}^{2M*1}$, $\hat{\boldsymbol{v}} = \left[\hat{\boldsymbol{v}}_1^{\mathrm{T}}, \cdots, \hat{\boldsymbol{v}}_M^{\mathrm{T}}\right]^{\mathrm{T}} \in \boldsymbol{R}^{2M*1}$, $\hat{\boldsymbol{a}} = \left[\hat{\boldsymbol{a}}_1^{\mathrm{T}}, \cdots, \hat{\boldsymbol{a}}_M^{\mathrm{T}}\right]^{\mathrm{T}} \in \boldsymbol{R}^{2M*1}$, $\bar{\boldsymbol{\eta}}_k = \left[\boldsymbol{\eta}_{M+1}^{\mathrm{T}}, \cdots, \boldsymbol{\eta}_N^{\mathrm{T}}\right]^{\mathrm{T}} \in \boldsymbol{R}^{2(N-M)*1}$, $\bar{\boldsymbol{v}}_k = \left[\boldsymbol{v}_{M+1}^{\mathrm{T}}, \cdots, \boldsymbol{v}_N^{\mathrm{T}}\right]^{\mathrm{T}} \in \boldsymbol{R}^{2(N-M)*1}$, $\bar{\boldsymbol{a}}_k = \left[\boldsymbol{a}_{M+1}^{\mathrm{T}}, \cdots, \boldsymbol{a}_N^{\mathrm{T}}\right]^{\mathrm{T}} \in \boldsymbol{R}^{2(N-M)*1}$, $\gamma = \left[\gamma_1, \cdots, \gamma_M\right]^{\mathrm{T}} \in \boldsymbol{R}^M$, and $\hat{\gamma} = \left[\hat{\gamma}_1, \cdots, \hat{\gamma}_M\right]^{\mathrm{T}} \in \boldsymbol{R}^M$. Moreover, $\boldsymbol{L}_1$ and $\boldsymbol{L}_2$ are block matrices within the Laplacian matrix.

Equation (12) can be compactly represented in the following vector form:

$$\begin{cases} \dot{\hat{\boldsymbol{\eta}}} = -k_1\mu_1(t)\tilde{\boldsymbol{\eta}} + \hat{\boldsymbol{v}} \\ \dot{\hat{\boldsymbol{v}}} = -k_2\mu_1(t)\tilde{\boldsymbol{v}} + \hat{\boldsymbol{a}} \\ \dot{\hat{\boldsymbol{a}}} = -k_3\mu_1(t)\tilde{\boldsymbol{a}} - \bar{\gamma} \\ \dot{\hat{\gamma}} = \bar{\boldsymbol{a}} - \mu_1(t)\hat{\gamma} \end{cases} \tag{15}$$

where $\bar{\gamma} = \left[\hat{\gamma}_1 \mathrm{sign}^{\mathrm{T}}(\tilde{\boldsymbol{a}}_1), \cdots, \hat{\gamma}_M \mathrm{sign}^{\mathrm{T}}(\tilde{\boldsymbol{a}}_M)\right]^{\mathrm{T}}$, $\bar{\boldsymbol{a}} = \left[\left\|\tilde{\boldsymbol{a}}_1\right\|_2, \cdots, \left\|\tilde{\boldsymbol{a}}_M\right\|_2\right]^{\mathrm{T}}$.

By differentiating Equation (14) and substituting Equation (15) into it, the derivative of the observation errors is expressed as

$$\begin{cases} \dot{\tilde{\boldsymbol{\eta}}} = -k_1\mu_1(t)(\boldsymbol{L}_1 \otimes \boldsymbol{I}_2)\tilde{\boldsymbol{\eta}} + \tilde{\boldsymbol{v}} \\ \dot{\tilde{\boldsymbol{v}}} = -k_2\mu_1(t)(\boldsymbol{L}_1 \otimes \boldsymbol{I}_2)\tilde{\boldsymbol{v}} + \tilde{\boldsymbol{a}} \\ \dot{\tilde{\boldsymbol{a}}} = -k_3\mu_1(t)(\boldsymbol{L}_1 \otimes \boldsymbol{I}_2)\tilde{\boldsymbol{a}} - (\boldsymbol{L}_1 \otimes \boldsymbol{I}_2)\bar{\gamma} + (\boldsymbol{L}_2 \otimes \boldsymbol{I}_2)\dot{\bar{\boldsymbol{a}}}_k \\ \dot{\tilde{\gamma}} = -\bar{\boldsymbol{a}} + \mu_1(t)\hat{\gamma} \end{cases} \tag{16}$$

Theorem 1 Under Assumptions 1 and 2, and employing the distributed prescribed-time observer and adaptive estimator detailed in Equation (12) for each follower, the observation errors as described by Equation (14) are guaranteed to converge to a small neighborhood of the origin within a prescribed time T_1. This convergence is guaranteed to be at the prescribed time provided that the parameters meet $k_1 > 1/2\lambda_{\min}(\boldsymbol{L}_1), k_2 > 1/2\lambda_{\min}(\boldsymbol{L}_1)$, and $k_3 > 0$, where $\boldsymbol{L}_1$ is the Laplace matrix of the followers.

Proof

To prove the convergence of the variable $\tilde{\boldsymbol{a}}$, a Lyapunov function is established as

$$\boldsymbol{V}_{\tilde{a}} = \frac{1}{2}\tilde{\boldsymbol{a}}^{\mathrm{T}}(\boldsymbol{L}_1 \otimes \boldsymbol{I}_2)^{-1}\tilde{\boldsymbol{a}} + \frac{1}{2}\tilde{\gamma}^{\mathrm{T}}\tilde{\gamma} \tag{17}$$

By taking the derivative of $\boldsymbol{V}_{\tilde{a}}$ and substituting Equation (16) into it, we can derive

$$\begin{aligned} \dot{\boldsymbol{V}}_{\tilde{a}} = & -k_3\mu_1(t)\tilde{\boldsymbol{a}}^{\mathrm{T}}\tilde{\boldsymbol{a}} - \tilde{\boldsymbol{a}}^{\mathrm{T}}\bar{\gamma} + \tilde{\boldsymbol{a}}^{\mathrm{T}}(\boldsymbol{L}_1^{-1}\boldsymbol{L}_2 \otimes \boldsymbol{I}_2)\dot{\bar{\boldsymbol{a}}}_k + \\ & \tilde{\gamma}^{\mathrm{T}}(-\bar{\boldsymbol{a}} + \mu_1(t)\hat{\gamma}) = -k_3\mu_1(t)\tilde{\boldsymbol{a}}^{\mathrm{T}}\tilde{\boldsymbol{a}} - \\ & \sum_{i=1}^{M}\hat{\gamma}_i\tilde{\boldsymbol{a}}_i^{\mathrm{T}}\mathrm{sign}(\tilde{\boldsymbol{a}}_i) + \tilde{\boldsymbol{a}}^{\mathrm{T}}\widehat{\boldsymbol{a}'} - \sum_{i=1}^{M}\tilde{\gamma}_i\left\|\tilde{\boldsymbol{a}}_i\right\|_2 + \\ & \mu_1(t)\tilde{\gamma}^{\mathrm{T}}(\gamma - \tilde{\gamma}) \leqslant -k_3\mu_1(t)\tilde{\boldsymbol{a}}^{\mathrm{T}}\tilde{\boldsymbol{a}} - \\ & \sum_{i=1}^{M}\hat{\gamma}_i\left\|\tilde{\boldsymbol{a}}_i\right\|_2 + \sum_{i=1}^{M}\left\|\tilde{\boldsymbol{a}}_i\right\|_2\left\|\dot{\tilde{\boldsymbol{a}}}_k\right\|_2 - \sum_{i=1}^{M}\tilde{\gamma}_i\left\|\tilde{\boldsymbol{a}}_i\right\|_2 - \\ & \mu_1(t)\frac{\left\|\tilde{\gamma}\right\|_2^2}{2} + \mu_1(t)\frac{\left\|\gamma\right\|_2^2}{2} \end{aligned} \tag{18}$$

where $\widehat{\boldsymbol{a}'} = \left[-C_o(\dot{\tilde{\boldsymbol{a}}}_k^{\mathrm{T}})_1, \cdots, -C_o(\dot{\tilde{\boldsymbol{a}}}_k^{\mathrm{T}})_M\right]^{\mathrm{T}}, k = M+1, \cdots, N.$ According to Assumption 2, the following inequality holds:

$$\begin{aligned} \dot{\boldsymbol{V}}_{\tilde{a}} \leqslant & -k_3\mu_1(t)\lambda_{\max}(\boldsymbol{L}_1)\tilde{\boldsymbol{a}}^{\mathrm{T}}(\boldsymbol{L}_1 \otimes \boldsymbol{I}_2)^{-1}\tilde{\boldsymbol{a}} + \\ & \sum_{i=1}^{M}(\gamma_i - \hat{\gamma}_i)\left\|\tilde{\boldsymbol{a}}_i\right\|_2 - \sum_{i=1}^{M}\tilde{\gamma}_i\left\|\tilde{\boldsymbol{a}}_i\right\|_2 - \\ & \mu_1(t)\frac{\left\|\tilde{\gamma}\right\|_2^2}{2} + \mu_1(t)\frac{\left\|\gamma\right\|_2^2}{2} \leqslant \\ & -2k_3\mu_1(t)\lambda_{\max}(\boldsymbol{L}_1)\frac{1}{2}\tilde{\boldsymbol{a}}^{\mathrm{T}}(\boldsymbol{L}_1 \otimes \boldsymbol{I}_2)^{-1}\tilde{\boldsymbol{a}} - \\ & \mu_1(t)\frac{1}{2}\tilde{\gamma}^{\mathrm{T}}\tilde{\gamma} + \mu_1(t)\frac{\left\|\gamma\right\|_2^2}{2} \leqslant \\ & -\alpha_1\mu_1(t)\boldsymbol{V}_{\tilde{a}} + \mu_1(t)\Omega_1 \end{aligned} \tag{19}$$

where $\alpha_1 = \min\left\{2k_3\lambda_{\max}(\boldsymbol{L}_1), 1\right\}$ and $\Omega_1 = \left\|\gamma\right\|_2^2/2$. To guar-

antee that $\boldsymbol{\alpha}_1 > 0$, the selection of k_3 satisfies $k_3 > 0$.

Similar to the proof process in Song et al. (2017), we can derive the following inequality:

$$\begin{aligned} \boldsymbol{V}_{\tilde{a}} \leqslant & \mathrm{e}^{-\alpha_1\int_{t_0}^{t}\mu_1(t)\mathrm{d}t}\boldsymbol{V}_{\tilde{a}}(t_0) + \Omega_1\int_{t_0}^{t}\mathrm{e}^{-\alpha_1\int_{\tau}^{t}\mu_1(\omega)\mathrm{d}\omega}\mu_1(\tau)\mathrm{d}\tau \leqslant \\ & \mathrm{e}^{-\alpha_1\int_{t_0}^{t}\mu_1(t)\mathrm{d}t}\boldsymbol{V}_{\tilde{a}}(t_0) + \frac{\Omega_1}{\alpha_1}\left(1 - \mathrm{e}^{-\alpha_1\int_{t_0}^{t}\mu_1(\omega)\mathrm{d}\omega}\right) \leqslant \\ & \mathrm{e}^{-\alpha_1\int_{t_0}^{t}\mu_1(t)\mathrm{d}t}\boldsymbol{V}_{\tilde{a}}(t_0) + \frac{\Omega_1}{\alpha_1} \end{aligned} \tag{20}$$

In this case, the following inequality holds:

$$\begin{aligned} \left\|\tilde{\boldsymbol{a}}\right\|_2 \leqslant & \sqrt{2\left(\mathrm{e}^{-\alpha_1\int_{t_0}^{t}\mu_1(t)\mathrm{d}t}\boldsymbol{V}_{\tilde{a}}(t_0) + \frac{\Omega_1}{\alpha_1}\right)} \leqslant \\ & \sqrt{2\left(V_{\tilde{a}}(t_0) + \frac{\Omega_1}{\alpha_1}\right)} = \Omega_2 \end{aligned} \tag{21}$$

Given that $\lim\limits_{t\to T_1^-}\mathrm{e}^{-\alpha_1\int_{t_0}^{t}\mu_1(t)\mathrm{d}t} = 0$, when $t \in \left[0, T_1\right)$, we can derive

$$\lim_{t\to T_1^-}\boldsymbol{V}_{\tilde{a}}(t) \leqslant \frac{\Omega_1}{\alpha_1} \tag{22}$$

After choosing $\mu_1(t) = 1$ when $t \in \left[T_1, +\infty\right)$, we can then derive the following:

$$\dot{\boldsymbol{V}}_{\tilde{a}} \leqslant -\alpha_1\boldsymbol{V}_{\tilde{a}} + \Omega_1 \tag{23}$$

Through integrating both sides of the abovementioned equation, we have

$$\boldsymbol{V}_{\tilde{a}}(t) \leqslant \left(\boldsymbol{V}_{\tilde{a}}(T_1) - \frac{\Omega_1}{\alpha_1}\right)\mathrm{e}^{-\alpha_1 t} + \frac{\Omega_1}{\alpha_1} \leqslant \frac{\Omega_1}{\alpha_1} \tag{24}$$

As a result, the variable $\left\|\tilde{\boldsymbol{a}}\right\|_2$ can converge to the neighborhood $\sqrt{\frac{2\Omega_1}{\alpha_1}}$ of the origin after a prescribed-time T_1.

To prove the convergence of variable $\tilde{\boldsymbol{v}}$, a Lyapunov function is constructed as

$$\boldsymbol{V}_{\tilde{v}} = \frac{1}{2}\tilde{\boldsymbol{v}}^{\mathrm{T}}\tilde{\boldsymbol{v}} \tag{25}$$

By taking the derivative concerning $\boldsymbol{V}_{\tilde{v}}$ and substituting Equation (16), we can derive

$$\begin{aligned} \dot{\boldsymbol{V}}_{\tilde{v}} = & -k_2\mu_1(t)\tilde{\boldsymbol{v}}^{\mathrm{T}}(\boldsymbol{L}_1 \otimes \boldsymbol{I}_2)\tilde{\boldsymbol{v}} + \tilde{\boldsymbol{v}}^{\mathrm{T}}\tilde{\boldsymbol{a}} \leqslant \\ & -k_2\mu_1(t)\lambda_{\min}(\boldsymbol{L}_1)\left\|\tilde{\boldsymbol{v}}\right\|_2^2 + \left\|\tilde{\boldsymbol{v}}\right\|_2\left\|\tilde{\boldsymbol{a}}\right\|_2 \end{aligned} \tag{26}$$

Given that $-\left\|\tilde{\boldsymbol{v}}\right\|_2^2 \leqslant 0$, we can derive that

$$\dot{\boldsymbol{V}}_{\tilde{v}} \leqslant \left\|\tilde{\boldsymbol{v}}\right\|_2\left\|\tilde{\boldsymbol{a}}\right\|_2 \leqslant \Omega_3\sqrt{\boldsymbol{V}_{\tilde{v}}}, \Omega_3 = \sqrt{2}\,\Omega_2 \tag{27}$$

By integrating both sides of the abovementioned equation, we have

$$\boldsymbol{V}_{\tilde{v}}(t) \leqslant \left(\frac{\Omega_3 t}{2} + \sqrt{\boldsymbol{V}_{\tilde{v}}(0)}\right)^2 \tag{28}$$

From the aforementioned equation, $\left\|\tilde{\boldsymbol{v}}\right\|_2$ will not escape to infinity within T_1 because Ω_3 and $\boldsymbol{V}_{\tilde{v}}(0)$ are bounded.

According to Equation (26), due to $\mu_1(t) \geqslant 1$, we further have

$$\begin{aligned} \dot{\boldsymbol{V}}_{\tilde{v}} \leqslant & -\mu_1(t)\left(k_2\lambda_{\min}(\boldsymbol{L}_1) - \frac{1}{2}\right)\left\|\tilde{\boldsymbol{v}}\right\|_2^2 + \frac{\left\|\tilde{\boldsymbol{a}}\right\|_2^2}{2} \leqslant \\ & -\alpha_2\mu_1(t)\boldsymbol{V}_{\tilde{v}} + \frac{\Omega_2^2}{2} \end{aligned} \tag{29}$$

where $\alpha_2 = 2k_2\lambda_{\min}(\boldsymbol{L}_1) - 1$. To ensure $\alpha_2 > 0$, the selection of k_2 satisfies $k_2 > 1/2\lambda_{\min}(\boldsymbol{L}_1)$.

Similarly, according to Equation (29), we can derive

$$\boldsymbol{V}_{\tilde{v}}(t) \leqslant \mathrm{e}^{-\alpha_2\int_{t_0}^{t}\mu_1(t)\mathrm{d}t}\boldsymbol{V}_{\tilde{v}}(0) + \frac{\Omega_2^2}{2}\mathrm{e}^{-\alpha_2\int_{t_0}^{t}\mu_1(t)\mathrm{d}t}\int_{t_0}^{t}\mathrm{e}^{\alpha_2\int_{t_0}^{t}\mu_1(\tau)\mathrm{d}\tau}\mathrm{d}\tau \tag{30}$$

Given that $\lim\limits_{t\to T_1^-}\mathrm{e}^{-\alpha_2\int_{t_0}^{t}\mu_1(t)\mathrm{d}t} = 0$, we can obtain

$$\boldsymbol{V}_{\tilde{v}}(t) \leqslant \boldsymbol{V}_{\tilde{v}}(0) + \frac{\Omega_2^2}{2} \tag{31}$$

Thus, from Equation (30), we have

$$\lim_{t\to T_1^-}\boldsymbol{V}_{\tilde{v}}(t) = 0 \tag{32}$$

Considering that $\mu_1(t) = 1$ when $t \in \left[T_1, +\infty\right)$, then

$$\dot{\boldsymbol{V}}_{\tilde{v}} \leqslant -\alpha_2\boldsymbol{V}_{\tilde{v}} + \frac{\Omega_2^2}{2} \tag{33}$$

Given that $\frac{\left\|\tilde{\boldsymbol{a}}\right\|_2^2}{2} \leqslant \frac{\Omega_1}{\alpha_1}$ when $t \in [T_1, +\infty)$, the integral of the abovementioned equation yields

$$\boldsymbol{V}_{\tilde{v}}(t) \leqslant \left(\boldsymbol{V}_{\tilde{v}}(T_1) - \frac{\Omega_1}{\alpha_1\alpha_2}\right)\mathrm{e}^{-\alpha_2 t} + \frac{\Omega_1}{\alpha_1\alpha_2} \leqslant \frac{\Omega_1}{\alpha_1\alpha_2} \tag{34}$$

As a result, the variable $\left\|\tilde{\boldsymbol{v}}\right\|_2$ can converge to the neighborhood $\sqrt{\frac{2\Omega_1}{\alpha_1\alpha_2}}$ of the origin after T_1.

To prove the convergence of variable $\tilde{\boldsymbol{\eta}}$, a Lyapunov function is constructed as

$$\boldsymbol{V}_{\tilde{\eta}} = \frac{1}{2}\tilde{\boldsymbol{\eta}}^{\mathrm{T}}\tilde{\boldsymbol{\eta}} \tag{35}$$

By taking the derivative concerning $\boldsymbol{V}_{\tilde{\eta}}$ and substituting Equation (16), we have

$$\begin{aligned}\dot{\boldsymbol{V}}_{\tilde{\eta}} = & -k_1\mu_1(t)\tilde{\boldsymbol{\eta}}^{\mathrm{T}}(\boldsymbol{L}_1 \otimes \boldsymbol{I}_2)\tilde{\boldsymbol{\eta}} + \tilde{\boldsymbol{\eta}}^{\mathrm{T}}\tilde{\boldsymbol{v}} \leqslant \\ & -k_1\mu_1(t)\lambda_{\min}(\boldsymbol{L}_1)\tilde{\boldsymbol{\eta}}^{\mathrm{T}}\tilde{\boldsymbol{\eta}} + \left\|\tilde{\boldsymbol{\eta}}\right\|_2\left\|\tilde{\boldsymbol{v}}\right\|_2\end{aligned} \tag{36}$$

According to Equations (21), (30), and (34), we have

$$\left\|\tilde{\boldsymbol{v}}\right\|_2 \leqslant \sqrt{2}\sqrt{\boldsymbol{V}_{\tilde{v}}(0) + \boldsymbol{V}_{\tilde{a}}(0) + \frac{\Omega_1 + \alpha_2\Omega_1}{\alpha_1\alpha_2}} \tag{37}$$

Given that $\dot{\boldsymbol{V}}_{\tilde{\eta}} \leqslant \left\|\tilde{\boldsymbol{\eta}}\right\|_2\left\|\tilde{\boldsymbol{v}}\right\|_2 \leqslant \Omega_4\sqrt{\boldsymbol{V}_{\tilde{\eta}}}$, $\Omega_4 = 2\sqrt{\boldsymbol{V}_{\tilde{v}}(0) + \boldsymbol{V}_{\tilde{a}}(0) + \frac{\Omega_1 + \alpha_2\Omega_1}{\alpha_1\alpha_2}}$, we have

$$\boldsymbol{V}_{\tilde{\eta}}(t) \leqslant \left(\frac{\Omega_4 t}{2} + \sqrt{V_{\tilde{\eta}}(0)}\right)^2 \tag{38}$$

Therefore, $\left\|\tilde{\boldsymbol{\eta}}\right\|_2$ will not escape to infinity within T_1, given that Ω_4 and $\boldsymbol{V}_{\tilde{\eta}}(0)$ are bounded.

According to Equation (36), we further have

$$\begin{aligned}\dot{\boldsymbol{V}}_{\tilde{\eta}} \leqslant & -\mu_1(t)\left(k_1\lambda_{\min}(\boldsymbol{L}_1) - \frac{1}{2}\right)\left\|\tilde{\boldsymbol{\eta}}\right\|_2^2 + \frac{\left\|\tilde{\boldsymbol{v}}\right\|_2^2}{2} \leqslant \\ & -\alpha_3\mu_1(t)\boldsymbol{V}_{\tilde{\eta}} + \frac{\Omega_4^2}{4}\end{aligned} \tag{39}$$

where $\alpha_3 = 2k_1\lambda_{\min}(\boldsymbol{L}_1) - 1$. To guarantee that $\alpha_3 > 0$, the selection of k_1 satisfies $k_1 > 1/2\lambda_{\min}(\boldsymbol{L}_1)$.

The integral of the abovementioned equation yields

$$\boldsymbol{V}_{\tilde{\eta}}(t) \leqslant \mathrm{e}^{-\alpha_3\int_{t_0}^{t}\mu_1(t)\mathrm{d}t}\boldsymbol{V}_{\tilde{\eta}}(0) + \frac{\Omega_4^2}{4}\mathrm{e}^{-\alpha_3\int_{t_0}^{t}\mu_1(t)\mathrm{d}t}\int_{t_0}^{t}\mathrm{e}^{\alpha_3\int_{t_0}^{t}\mu_1(\tau)\mathrm{d}\tau}\mathrm{d}\tau \tag{40}$$

Similarly, given that $\lim\limits_{t\to T_1^-}\mathrm{e}^{-\alpha_3\int_{t_0}^{t}\mu_1(t)\mathrm{d}t} = 0$, we have

$$\lim_{t\to T_1^-}\boldsymbol{V}_{\tilde{\eta}}(t) = 0 \tag{41}$$

Given that $\mu_1(t) = 1$ and $\frac{\left\|\tilde{\boldsymbol{v}}\right\|_2^2}{2} \leqslant \frac{\Omega_1}{\alpha_1\alpha_2}$ when $t \in \left[T_1, +\infty\right)$, we have

$$\dot{\boldsymbol{V}}_{\tilde{\eta}} \leqslant -\alpha_3\boldsymbol{V}_{\tilde{\eta}} + \frac{\Omega_1}{\alpha_1\alpha_2} \tag{42}$$

After integrating the two sides of the abovementioned equation, we can obtain

$$\begin{aligned}\boldsymbol{V}_{\tilde{\eta}}(t) \leqslant & \left(\boldsymbol{V}_{\tilde{\eta}}(T_1) - \frac{\Omega_1}{\alpha_1\alpha_2\alpha_3}\right)\mathrm{e}^{-\alpha_3 t} + \frac{\Omega_1}{\alpha_1\alpha_2\alpha_3} \leqslant \\ & \frac{\Omega_1}{\alpha_1\alpha_2\alpha_3} = \frac{\left\|\boldsymbol{\gamma}\right\|_2^2}{2\alpha_1\alpha_2\alpha_3}\end{aligned} \tag{43}$$

As a result, the variable $\left\|\tilde{\boldsymbol{\eta}}\right\|_2$ can converge to the neighborhood $\sqrt{\frac{1}{\alpha_1\alpha_2\alpha_3}}\left\|\boldsymbol{\gamma}\right\|$ of the origin after T_1.

Therefore, under the effect of the distributed observer and the adaptive estimator Equation (12), the position, velocity, and acceleration observation errors of each follower relative to the convex hull formed by the virtual leaders will asymptotically converge and remain bounded within T_1. The proof of Theorem 1 has been successfully constructed in this section.

3.2 Improved PTESO

Similar to the PTESO in Cui and Jin (2021), the observer designed in this study does not require the velocity information of USVs. Notably, general uncertainties exist in the dynamic model of USVs using the position and heading information available from the USV. First, the term for general uncertainties $\boldsymbol{f}_i$ is extended by $\boldsymbol{x}_{3i}$. Consequently, the extended state system is described by

$$\begin{cases}\dot{\boldsymbol{x}}_{1i} = \boldsymbol{R}_i(\boldsymbol{\psi}_i)\boldsymbol{x}_{2i} \\ \dot{\boldsymbol{x}}_{2i} = \boldsymbol{M}_i^{*-1}\mathrm{sat}(\boldsymbol{\tau}_i) + \boldsymbol{x}_{3i} \\ \dot{\boldsymbol{x}}_{3i} = \dot{\boldsymbol{f}}_i\end{cases} \tag{44}$$

$\hat{\boldsymbol{x}}_{1i}$, $\hat{\boldsymbol{x}}_{2i}$, and $\hat{\boldsymbol{x}}_{3i}$ denote the observed variables of $\boldsymbol{x}_{1i}$, $\boldsymbol{x}_{2i}$, and $\boldsymbol{x}_{3i}$ for each follower. The structure of modified PTESO is constructed as

$$\begin{cases}\dot{\hat{\boldsymbol{x}}}_{1i} = \boldsymbol{R}_i(\boldsymbol{\psi}_i)\hat{\boldsymbol{x}}_{2i} + \left(k_{1i}\mu_2(t)l_1\boldsymbol{I}_3\right)\left(\boldsymbol{\eta}_i - \hat{\boldsymbol{x}}_{1i}\right) - \\ \qquad \hat{r}\boldsymbol{R}_i(\boldsymbol{\psi}_i)\boldsymbol{S}\boldsymbol{R}_i^{\mathrm{T}}(\boldsymbol{\psi}_i)\left(\boldsymbol{\eta}_i - \hat{\boldsymbol{x}}_{1i}\right) \\ \dot{\hat{\boldsymbol{x}}}_{2i} = \hat{\boldsymbol{x}}_{3i} + \boldsymbol{M}_i^{*-1}\mathrm{sat}(\boldsymbol{\tau}_i) + k_{1i}^2\mu_2^2(t)l_2\boldsymbol{R}_i^{\mathrm{T}}(\boldsymbol{\psi}_i)\left(\boldsymbol{\eta}_i - \hat{\boldsymbol{x}}_{1i}\right) \\ \dot{\hat{\boldsymbol{x}}}_{3i} = k_{1i}^3\mu_2^3(t)l_3\boldsymbol{R}_i^{\mathrm{T}}(\boldsymbol{\psi}_i)\left(\boldsymbol{\eta}_i - \hat{\boldsymbol{x}}_{1i}\right)\end{cases} \tag{45}$$

where $\hat{\boldsymbol{r}} = \hat{\boldsymbol{x}}_{2i}^{\mathrm{T}}\boldsymbol{q} \in \boldsymbol{R}$, $\boldsymbol{q} = [0, 0, 1]^{\mathrm{T}}$. The parameters k_{1i}, l_1, l_2, and l_3 will be designed in Theorem 2.

The observation error variables are defined as follows:

$$\begin{cases}\boldsymbol{e}_{1i} = \boldsymbol{R}_i^{\mathrm{T}}(\boldsymbol{\psi}_i)\left(\boldsymbol{\eta}_i - \hat{\boldsymbol{x}}_{1i}\right) \\ \boldsymbol{e}_{2i} = \boldsymbol{v}_i - \hat{\boldsymbol{x}}_{2i} \\ \boldsymbol{e}_{3i} = \boldsymbol{f}_i - \hat{\boldsymbol{x}}_{3i}\end{cases} \tag{46}$$

By taking the derivative of the abovementioned equation and substituting Equation (45), we have

$$\begin{cases} \dot{\boldsymbol{e}}_{1i} = \boldsymbol{e}_{2i} - \left(k_{1i}\mu_2(t) l_1 \otimes \boldsymbol{I}_3\right)\boldsymbol{e}_{1i} + \tilde{r}_i \boldsymbol{S}\boldsymbol{e}_{1i} \\ \dot{\boldsymbol{e}}_{2i} = \boldsymbol{e}_{3i} - k_{1i}{}^2\mu_2^2(t) l_2 \boldsymbol{e}_{1i} \\ \dot{\boldsymbol{e}}_{3i} = \dot{\boldsymbol{f}}_i - k_{1i}{}^3\mu_2^3(t) l_3 \boldsymbol{e}_{1i} \end{cases} \tag{47}$$

where $\tilde{r}_i = \hat{r}_i - r_i$.

$\boldsymbol{E} = \left[\boldsymbol{e}_{1i}^{\mathrm{T}}, \boldsymbol{e}_{2i}^{\mathrm{T}}, \boldsymbol{e}_{3i}^{\mathrm{T}}\right]^{\mathrm{T}}$ and $\boldsymbol{W} = \left[\tilde{r}_i \boldsymbol{e}_{1i}^{\mathrm{T}} \boldsymbol{S}^{\mathrm{T}}, \boldsymbol{0}_{3\times 1}^{\mathrm{T}}, \dot{\boldsymbol{f}}_i^{\mathrm{T}}\right]^{\mathrm{T}}$ are defined, and Equation (47) is introduced into the following vector form:

$$\dot{\boldsymbol{E}} = \left(\boldsymbol{A} \otimes \boldsymbol{I}_3\right)\boldsymbol{E} - \left(\boldsymbol{\psi}\boldsymbol{L}\boldsymbol{C} \otimes \boldsymbol{I}_3\right)\boldsymbol{E} + \boldsymbol{W} \tag{48}$$

where $\boldsymbol{A} = \begin{bmatrix} 0 & 1 & 0 \\ 0 & 0 & 1 \\ 0 & 0 & 0 \end{bmatrix}$, $\boldsymbol{\psi} = \mathrm{diag}\left\{k_{1i}\mu_2(t), k_{1i}^2\mu_2^2(t), k_{1i}^3\mu_2^3(t)\right\}$, $\boldsymbol{L} = \left[l_1, l_2, l_3\right]^{\mathrm{T}}$, and $\boldsymbol{C} = \left[1, 0, 0\right]$.

$\tilde{\boldsymbol{\psi}} = \mathrm{diag}\left\{k_{1i}^3\mu_2^3(t), k_{1i}^2\mu_2^2(t), k_{1i}\mu_2(t)\right\}$ and $\tilde{\boldsymbol{\varphi}} = \left(\tilde{\boldsymbol{\psi}} \otimes \boldsymbol{I}_3\right)\boldsymbol{E}$ are defined. Then, we have

$$\boldsymbol{E} = \left(\tilde{\boldsymbol{\psi}} \otimes \boldsymbol{I}_3\right)^{-1}\tilde{\boldsymbol{\varphi}} \tag{49}$$

$$\dot{\tilde{\boldsymbol{\psi}}} = \rho\mu_2(t)\boldsymbol{D}\tilde{\boldsymbol{\psi}} \tag{50}$$

where $\boldsymbol{D} = \mathrm{diag}\left\{3, 2, 1\right\}$ and $\rho = 1/T_2$.

By taking the derivative concerning $\tilde{\boldsymbol{\varphi}}$, we have

$$\begin{aligned} \dot{\tilde{\boldsymbol{\varphi}}} = &\left(\dot{\tilde{\boldsymbol{\psi}}} \otimes \boldsymbol{I}_3\right)\boldsymbol{E} + \left(\tilde{\boldsymbol{\psi}} \otimes \boldsymbol{I}_3\right)\dot{\boldsymbol{E}} = \\ &\left(\rho\mu_2(t)\boldsymbol{D}\tilde{\boldsymbol{\psi}} \otimes \boldsymbol{I}_3\right)\left(\tilde{\boldsymbol{\psi}} \otimes \boldsymbol{I}_3\right)^{-1}\tilde{\boldsymbol{\varphi}} + \\ &\left(\tilde{\boldsymbol{\psi}} \otimes \boldsymbol{I}_3\right)\left[\left(\boldsymbol{A} \otimes \boldsymbol{I}_3\right)\boldsymbol{E} - \left(\boldsymbol{\psi}\boldsymbol{L}\boldsymbol{C} \otimes \boldsymbol{I}_3\right)\boldsymbol{E} + \boldsymbol{W}\right] = \\ &\rho\mu_2(t)\left(\boldsymbol{D} \otimes \boldsymbol{I}_3\right)\tilde{\boldsymbol{\varphi}} + \left(\tilde{\boldsymbol{\psi}} \otimes \boldsymbol{I}_3\right)\left(\boldsymbol{A} \otimes \boldsymbol{I}_3\right)\left(\tilde{\boldsymbol{\psi}} \otimes \boldsymbol{I}_3\right)^{-1}\tilde{\boldsymbol{\varphi}} - \\ &\left(\tilde{\boldsymbol{\psi}} \otimes \boldsymbol{I}_3\right)\left(\boldsymbol{\psi}\boldsymbol{L}\boldsymbol{C} \otimes \boldsymbol{I}_3\right)\left(\tilde{\boldsymbol{\psi}} \otimes \boldsymbol{I}_3\right)^{-1}\tilde{\boldsymbol{\varphi}} + \left(\tilde{\boldsymbol{\psi}} \otimes \boldsymbol{I}_3\right)\boldsymbol{W} = \\ &\rho\mu_2(t)\left(\boldsymbol{D} \otimes \boldsymbol{I}_3\right)\tilde{\boldsymbol{\varphi}} + \left(\tilde{\boldsymbol{\psi}}\boldsymbol{A}\tilde{\boldsymbol{\psi}}^{-1} \otimes \boldsymbol{I}_3\right)\tilde{\boldsymbol{\varphi}} - \\ &\left(\tilde{\boldsymbol{\psi}}\boldsymbol{\psi}\boldsymbol{L}\boldsymbol{C}\tilde{\boldsymbol{\psi}}^{-1} \otimes \boldsymbol{I}_3\right)\tilde{\boldsymbol{\varphi}} + \left(\tilde{\boldsymbol{\psi}} \otimes \boldsymbol{I}_3\right)\boldsymbol{W} \end{aligned} \tag{51}$$

Owing to the properties of $\tilde{\boldsymbol{\psi}}$, the following relationship holds:

$$\begin{cases} \tilde{\boldsymbol{\psi}}\boldsymbol{A}\tilde{\boldsymbol{\psi}}^{-1} = k_{1i}\mu_2(t)\boldsymbol{A} \\ \tilde{\boldsymbol{\psi}}\boldsymbol{\psi}\boldsymbol{L}\boldsymbol{C}\tilde{\boldsymbol{\psi}}^{-1} = k_{1i}\mu_2(t)\boldsymbol{L}\boldsymbol{C} \end{cases} \tag{52}$$

Substituting the abovementioned equation into Equation (51) yields

$$\begin{aligned} \dot{\tilde{\boldsymbol{\varphi}}} = &\rho\mu_2(t)\left(\boldsymbol{D} \otimes \boldsymbol{I}_3\right)\tilde{\boldsymbol{\varphi}} + k_{1i}\mu_2(t)\left(\boldsymbol{A} \otimes \boldsymbol{I}_3\right)\tilde{\boldsymbol{\varphi}} - \\ &k_{1i}\mu_2(t)\left(\boldsymbol{L}\boldsymbol{C} \otimes \boldsymbol{I}_3\right)\tilde{\boldsymbol{\varphi}} + \left(\tilde{\boldsymbol{\psi}} \otimes I_3\right)\boldsymbol{W} \end{aligned} \tag{53}$$

Theorem 2 Under Assumption 3, and utilizing the PTESO detailed in Equation (45) for the follower, the observation errors for the general uncertainties in Equation (46) will converge to a small neighborhood around the origin within a prescribed time T_2. This convergence is guaranteed to be at the prescribed time provided that the parameters satisfy $k_{1i} \geqslant \rho\lambda_{p\max} + 4\bar{\boldsymbol{P}}_1\left\|\tilde{\boldsymbol{r}}_i\right\|_2\left\|\boldsymbol{S}\right\|_2$, $\xi \geqslant 2$, $l_1 > 0, l_2 > 0, l_3 > 0$, and $l_1 l_2 > l_3$.

Proof

A Lyapunov function is formulated in the following manner:

$$\boldsymbol{V}_{\tilde{\varphi}} = \tilde{\boldsymbol{\varphi}}^{\mathrm{T}}\left(\boldsymbol{P} \otimes \boldsymbol{I}_3\right)\tilde{\boldsymbol{\varphi}} \tag{54}$$

By taking the derivative concerning $\boldsymbol{V}_{\tilde{\varphi}}$ and substituting Equation (53), we obtain

$$\begin{aligned} \dot{\boldsymbol{V}}_{\tilde{\varphi}} = &\dot{\tilde{\boldsymbol{\varphi}}}^{\mathrm{T}}\left(\boldsymbol{p} \otimes \boldsymbol{I}_3\right)\tilde{\boldsymbol{\varphi}} + \tilde{\boldsymbol{\varphi}}^{\mathrm{T}}\left(\boldsymbol{p} \otimes \boldsymbol{I}_3\right)\dot{\tilde{\boldsymbol{\varphi}}} = \\ &\rho\mu_2(t)\tilde{\boldsymbol{\varphi}}^{\mathrm{T}}\left[\left(\boldsymbol{D}^{\mathrm{T}}\boldsymbol{P} + \boldsymbol{P}\boldsymbol{D}\right) \otimes \boldsymbol{I}_3\right]\tilde{\boldsymbol{\varphi}} + \\ &k_{1i}\mu_2(t)\tilde{\boldsymbol{\varphi}}^{\mathrm{T}}\left[\left(\boldsymbol{A}^{\mathrm{T}}\boldsymbol{P} + \boldsymbol{P}\boldsymbol{A}\right) \otimes \boldsymbol{I}_3\right]\tilde{\boldsymbol{\varphi}} - \\ &k_{1i}\mu_2(t)\tilde{\boldsymbol{\varphi}}^{\mathrm{T}}\left\{\left[\left(\boldsymbol{L}\boldsymbol{C}\right)^{\mathrm{T}}\boldsymbol{P} + \boldsymbol{P}\left(\boldsymbol{L}\boldsymbol{C}\right)\right] \otimes \boldsymbol{I}_3\right\}\tilde{\boldsymbol{\varphi}} + \\ &\boldsymbol{W}^{\mathrm{T}}\left(\tilde{\boldsymbol{\psi}}^{\mathrm{T}}\boldsymbol{P} \otimes I_3\right)\tilde{\boldsymbol{\varphi}} + \tilde{\boldsymbol{\varphi}}^{\mathrm{T}}\left(\boldsymbol{P}\tilde{\boldsymbol{\psi}} \otimes \boldsymbol{I}_3\right)\boldsymbol{W} \end{aligned} \tag{55}$$

By using pole placement,

$$\boldsymbol{A} - \boldsymbol{L}\boldsymbol{C} = \begin{bmatrix} -l_1 & 1 & 0 \\ -l_2 & 0 & 1 \\ -l_3 & 0 & 0 \end{bmatrix}$$

is a Hurwitz matrix when $l_1 > 0, l_2 > 0, l_3 > 0$, and $l_1 l_2 > l_3$ are satisfied. The matrices $\boldsymbol{P}, \boldsymbol{A}, \boldsymbol{L}$, and $\boldsymbol{C}$ satisfy the linear matrix inequalities in Lemma 5 of Chang et al. (2021). From Lemma 3, we have

$$\begin{cases} \left(\boldsymbol{A} - \boldsymbol{L}\boldsymbol{C}\right)^{\mathrm{T}}\boldsymbol{P} + \boldsymbol{P}\left(\boldsymbol{A} - \boldsymbol{L}\boldsymbol{C}\right) \leqslant -\xi\boldsymbol{I}_3 \\ \lambda_{p\min}\boldsymbol{I}_3 \leqslant \boldsymbol{P}\boldsymbol{D} + \boldsymbol{D}\boldsymbol{P} \leqslant \lambda_{p\max}\boldsymbol{I}_3 \end{cases} \tag{56}$$

where $\lambda_{p\min}$ and $\lambda_{p\max}$ are the minimum and maximum positive eigenvalues of the matrix $\boldsymbol{P}\boldsymbol{D} + \boldsymbol{D}\boldsymbol{P}$, respectively.

Substituting the abovementioned inequality into Equation (55) derives

$$\begin{aligned} \dot{\boldsymbol{V}}_{\tilde{\varphi}} \leqslant &\rho\lambda_{p\max}\mu_2(t)\tilde{\boldsymbol{\varphi}}^{\mathrm{T}}\tilde{\boldsymbol{\varphi}} - \xi k_{1i}\mu_2(t)\tilde{\boldsymbol{\varphi}}^{\mathrm{T}}\tilde{\boldsymbol{\varphi}} + \\ &k_{1i}^3\mu_2^3(t)\left[\left(2\boldsymbol{P}_{11}\right)\tilde{\boldsymbol{r}}_i\boldsymbol{e}_{1i}^{\mathrm{T}}\boldsymbol{S}^{\mathrm{T}}\tilde{\boldsymbol{\varphi}}_1 + \left(2\boldsymbol{P}_{12}\right)\tilde{\boldsymbol{r}}_i\boldsymbol{e}_{1i}^{\mathrm{T}}\boldsymbol{S}^{\mathrm{T}}\tilde{\boldsymbol{\varphi}}_2 + \right. \\ &\left.\left(2\boldsymbol{P}_{13}\right)\tilde{\boldsymbol{r}}_i\boldsymbol{e}_{1i}^{\mathrm{T}}\boldsymbol{S}^{\mathrm{T}}\tilde{\boldsymbol{\varphi}}_3\right] + k_{1i}\mu_2(t)\left[\left(2\boldsymbol{P}_{13}\right)\dot{\boldsymbol{f}}_i{}^{\mathrm{T}}\tilde{\boldsymbol{\varphi}}_1 + \right. \\ &\left.\left(2\boldsymbol{P}_{23}\right)\dot{\boldsymbol{f}}_i{}^{\mathrm{T}}\tilde{\boldsymbol{\varphi}}_2 + \left(2\boldsymbol{P}_{33}\right)\dot{\boldsymbol{f}}_i{}^{\mathrm{T}}\tilde{\boldsymbol{\varphi}}_3\right] \end{aligned} \tag{57}$$

Given $\tilde{\boldsymbol{\varphi}}_1 = k_{1i}^3\mu_2^3(t)\boldsymbol{e}_{1i}$ and $\tilde{\boldsymbol{\varphi}}_1^{\mathrm{T}}\boldsymbol{S}^{\mathrm{T}}\tilde{\boldsymbol{\varphi}}_1 = 0$, we have

$$\begin{aligned}\dot{V}_{\tilde{\varphi}} \leqslant\ & \rho\lambda_{p\max}\mu_2(t)\left\|\tilde{\boldsymbol{\varphi}}\right\|_2 - \xi k_{1i}\mu_2(t)\left\|\tilde{\boldsymbol{\varphi}}\right\|_2 + \\ & \left[(2\boldsymbol{P}_{12})\tilde{\boldsymbol{r}}_i\tilde{\boldsymbol{\varphi}}^{\mathrm{T}}{}_1\boldsymbol{S}^{\mathrm{T}}\tilde{\boldsymbol{\varphi}}_2 + (2\boldsymbol{P}_{13})\tilde{\boldsymbol{r}}_i\tilde{\boldsymbol{\varphi}}^{\mathrm{T}}{}_1\boldsymbol{S}^{\mathrm{T}}\tilde{\boldsymbol{\varphi}}_3\right] + \\ & k_{1i}\mu_2(t)\left[(2\boldsymbol{P}_{13})\left\|\dot{\boldsymbol{f}}_i\right\|_2\left\|\tilde{\boldsymbol{\varphi}}_1\right\|_2 + (2\boldsymbol{P}_{23})\left\|\dot{\boldsymbol{f}}_i\right\|_2\left\|\tilde{\boldsymbol{\varphi}}_2\right\|_2 + \right. \\ & \left.(2P_{33})\left\|\dot{\boldsymbol{f}}_i\right\|_2\left\|\tilde{\boldsymbol{\varphi}}_3\right\|_2\right] \leqslant \rho\lambda_{p\max}\mu_2(t)\left\|\tilde{\boldsymbol{\varphi}}\right\|_2^2 - \\ & \xi k_{1i}\mu_2(t)\left\|\tilde{\boldsymbol{\varphi}}\right\|_2^2 + 4\bar{\boldsymbol{P}}_1\mu_2(t)\left\|\tilde{\boldsymbol{r}}_i\right\|_2\|\boldsymbol{S}\|_2\left\|\tilde{\boldsymbol{\varphi}}\right\|_2^2 + \\ & k_{1i}\mu_2(t)\left(3\left\|\bar{\boldsymbol{P}}_2\dot{\boldsymbol{f}}_i\right\|_2^2 + \left\|\tilde{\boldsymbol{\varphi}}\right\|_2^2\right) \leqslant \\ & -k_{1i}\mu_2(t)\left(\xi - \frac{\rho\lambda_{p\max} + 4\bar{\boldsymbol{P}}_1\left\|\tilde{\boldsymbol{r}}_i\right\|_2\|\boldsymbol{S}\|_2}{k_{1i}} - 1\right)\left\|\tilde{\boldsymbol{\varphi}}\right\|_2^2 + \\ & 3k_{1i}\mu_2(t)\left\|\bar{\boldsymbol{P}}_2\dot{\boldsymbol{f}}_i\right\|_2^2 \leqslant -\frac{k_{1i}\alpha_3}{\lambda_{\max}(\boldsymbol{P})}\mu_2(t)V_{\tilde{\varphi}} + \\ & 3k_{1i}\mu_2(t)\left\|\bar{\boldsymbol{P}}_2\dot{\boldsymbol{f}}_i\right\|_2^2 \leqslant -\alpha_4\mu_2(t)V_{\tilde{\varphi}} + \mu_2(t)\boldsymbol{\Delta}_1\end{aligned} \tag{58}$$

where $\bar{\boldsymbol{P}}_1 = \max\left\{\left|\boldsymbol{P}_{12}\right|, \left|\boldsymbol{P}_{13}\right|\right\}$, $\bar{\boldsymbol{P}}_2 = \max\left\{\left|\boldsymbol{P}_{13}\right|, \left|\boldsymbol{P}_{23}\right|, \left|\boldsymbol{P}_{33}\right|\right\}$, $\xi \geqslant 2$, $k_{1i} \geqslant \rho\lambda_{p\max} + 4\bar{\boldsymbol{P}}_1\left\|\tilde{\boldsymbol{r}}_i\right\|_2\|\boldsymbol{S}\|_2$, $\alpha_4 = \dfrac{k_{1i}\alpha_3}{\lambda_{\max}(\boldsymbol{P})}$, $\alpha_3 = \xi - \dfrac{\rho\lambda_{p\max} + 4\bar{\boldsymbol{P}}_1\left\|\tilde{\boldsymbol{r}}_i\right\|_2\|\boldsymbol{S}\|_2}{k_{1i}} - 1$, and $3k_{1i}\left\|\bar{\boldsymbol{P}}_2\dot{\boldsymbol{f}}_i\right\|_2^2 \leqslant \boldsymbol{\Delta}_1$.

To prove that $\left\|\tilde{\boldsymbol{r}}_i\right\|_2$ is bounded, the following proof process is provided.

According to Equation (47), we have

$$\begin{bmatrix}\dot{\boldsymbol{e}}_{1i}\\ \dot{\boldsymbol{e}}_{2i}\\ \dot{\boldsymbol{e}}_{3i}\end{bmatrix} = \begin{bmatrix}\tilde{\boldsymbol{r}}_i\boldsymbol{S} - \left(k_{1i}\mu_2(t)l_1 \otimes \boldsymbol{I}_3\right) & 1 & 0\\ -k_{1i}{}^2\mu_2^2(t)l_2 & 0 & 1\\ -k_{1i}{}^3\mu_2^3(t)l_3 & 0 & 0\end{bmatrix}\begin{bmatrix}\boldsymbol{e}_{1i}\\ \boldsymbol{e}_{2i}\\ \boldsymbol{e}_{3i}\end{bmatrix} + \begin{bmatrix}0\\ 0\\ \dot{\boldsymbol{f}}_i\end{bmatrix} \tag{59}$$

The characteristic equation of the state transition matrix is

$$\lambda^3 + \boldsymbol{a}\lambda^2 + \boldsymbol{b}\lambda + \boldsymbol{c} = 0 \tag{60}$$

where $\boldsymbol{a} = \left[\left(k_{1i}\mu_2(t)l_1 \otimes \boldsymbol{I}_3\right) - \tilde{\boldsymbol{r}}_i\boldsymbol{S}\right]$, $\boldsymbol{b} = k_{1i}^2\mu_2^2(t)l_2$, and $\boldsymbol{c} = k_{1i}^3\mu_2^3(t)l_3$.

The Hurwitz matrix for the polynomial is given as follows:

$$\boldsymbol{D}_i = \begin{bmatrix}\boldsymbol{a} & \boldsymbol{c} & 0\\ 1 & \boldsymbol{b} & 0\\ 0 & \boldsymbol{a} & \boldsymbol{c}\end{bmatrix} \tag{61}$$

where $\boldsymbol{a} = \begin{bmatrix}k_{1i}\mu_2(t)l_1 & \tilde{\boldsymbol{r}}_i & 0\\ -\tilde{\boldsymbol{r}}_i & k_{1i}\mu_2(t)l_1 & 0\\ 0 & 0 & k_{1i}\mu_2(t)l_1\end{bmatrix}$.

According to Definition 2, when $k_{1i}, l_1 > 0$ is satisfied, $\boldsymbol{a}$ is considered a positive-definite matrix. In this case, the first-order principal minor $\boldsymbol{\Delta}_1 = \boldsymbol{a}$ is positive. Similarly, when $l_1 l_2 > l_3$ is satisfied, the second-order principal minor $\boldsymbol{\Delta}_2 = \boldsymbol{ab} - \boldsymbol{c} = \left\{\left[k_{1i}\mu_2(t)\left(l_1 - l_3/l_2\right)\right] \otimes \boldsymbol{I}_3\right\} - \tilde{\boldsymbol{r}}_i\boldsymbol{S}$ is positive. When $l_3 > 0$ is satisfied, the third-order principal minor $\boldsymbol{\Delta}_3 = (\boldsymbol{ab} - \boldsymbol{c})\boldsymbol{c}$ is positive.

When all principal minors of $\boldsymbol{D}_i$ are positive, and considering the satisfaction of Assumption 3, the observation errors exhibit stable convergence and remain bounded. Therefore, $\left\|\tilde{\boldsymbol{r}}_i\right\|_2$ is bounded, and a parameter k_{1i} exists such that the condition $k_{1i} \geqslant \rho\lambda_{p\max} + 4\bar{\boldsymbol{P}}_1\left\|\tilde{\boldsymbol{r}}_i\right\|_2\|\boldsymbol{S}\|_2$ is satisfied.

When $t \in \left[0, T_2\right)$, we can similarly derive

$$\boldsymbol{V}_{\tilde{\varphi}} \leqslant \mathrm{e}^{-\alpha_4\int_{t_0}^{t}\mu_2(t)\mathrm{d}t}\boldsymbol{V}_{\tilde{\varphi}}(t_0) + \frac{\boldsymbol{\Delta}}{\alpha_4} \tag{62}$$

According to Equation (49), we have

$$\begin{aligned}\|\boldsymbol{E}\|^2 \leqslant & \left\|\left(\tilde{\boldsymbol{\psi}} \otimes \boldsymbol{I}_3\right)^{-1}\right\|_2^2\left\|\tilde{\boldsymbol{\varphi}}\right\|_2^2 \leqslant \frac{\left\|\left(\tilde{\boldsymbol{\psi}} \otimes \boldsymbol{I}_3\right)^{-1}\right\|_2^2}{\lambda_{\min}(\boldsymbol{P})}\boldsymbol{V}_{\tilde{\varphi}} \leqslant \\ & \frac{\left\|\left(\tilde{\boldsymbol{\psi}} \otimes \boldsymbol{I}_3\right)^{-1}\right\|_2^2}{\lambda_{\min}(\boldsymbol{P})}\left(\mathrm{e}^{-\alpha_4\int_{t_0}^{t}\mu_2(t)\mathrm{d}t}\boldsymbol{V}_{\tilde{\varphi}}(t_0) + \frac{\boldsymbol{\Delta}}{\alpha_4}\right)\end{aligned} \tag{63}$$

Given $\lim\limits_{t \to T_2}\left\|\left(\tilde{\boldsymbol{\psi}} \otimes \boldsymbol{I}_3\right)^{-1}\right\|_2^2 = 0$, the condition $\lim\limits_{t \to T_2}\|\boldsymbol{E}\|^2 = 0$ holds.

When $t \in \left[T_2, +\infty\right)$, given that $\mu_2(t) = 1$, we can derive

$$\dot{\boldsymbol{V}}_{\tilde{\varphi}} \leqslant -\alpha_4\boldsymbol{V}_{\tilde{\varphi}} + \boldsymbol{\Delta}_1 \tag{64}$$

After integrating both sides of the abovementioned equation, we can obtain

$$\boldsymbol{V}_{\tilde{\varphi}}(t) \leqslant \left(\boldsymbol{V}_{\tilde{\varphi}}(T_2) - \frac{\boldsymbol{\Delta}_1}{\alpha_4}\right)\mathrm{e}^{-\alpha_4 t} + \frac{\boldsymbol{\Delta}_1}{\alpha_4} \leqslant \frac{\boldsymbol{\Delta}_1}{\alpha_4} \tag{65}$$

Similarly, we can derive

$$\|\boldsymbol{E}\|^2 \leqslant \frac{\lambda_{\max}^2(\tilde{\boldsymbol{\psi}}_k^{-1})}{\lambda_{\min}(\boldsymbol{P})}\frac{\boldsymbol{\Delta}_1}{\alpha_4} \tag{66}$$

where $\tilde{\boldsymbol{\psi}}_k = \mathrm{diag}\left\{k_{1i}, k_{1i}^2, k_{1i}^3\right\}$ is a positive-definite constant matrix.

Therefore, the observation errors of the PTESO for the total disturbance term remain bounded within T_2, that is, $\left\|\boldsymbol{e}_{3i}\right\|^2 \leqslant \dfrac{\lambda_{\max}^2(\tilde{\boldsymbol{\psi}}_k^{-1})}{\lambda_{\min}(\boldsymbol{P})}\dfrac{\boldsymbol{\Delta}_1}{\alpha_4}$. The proof of Theorem 2 is completed.

3.3 Prescribed-time command filter

To avoid using the differential signal of the virtual guidance protocol, the PTCF is designed as follows:

$$\begin{cases}\dot{\bar{\boldsymbol{v}}}_{ir}=\bar{\boldsymbol{v}}_{id}-k_{p1}\mu_2(t)\left(\bar{\boldsymbol{v}}_{ir}-\bar{\alpha}_i\right)-\dot{\mu}_2(t)\mu_2^{-1}(t)\left(\bar{\boldsymbol{v}}_{ir}-\bar{\alpha}_i\right)\\ \dot{\bar{\boldsymbol{v}}}_{id}=-k_{p2}\mu_2^2(t)\left(\bar{\boldsymbol{v}}_{ir}-\bar{\alpha}_i\right)\end{cases} \tag{67}$$

where $\bar{\boldsymbol{v}}_{ir}\in\boldsymbol{R}^2$ and $\bar{\boldsymbol{v}}_{id}\in\boldsymbol{R}^2$ are the estimates of the virtual control signal $\bar{\alpha}_i$ and $\dot{\bar{\alpha}}_i$; k_{p1}, k_{p2} are suitable positive constants.

By defining $\tilde{\bar{\boldsymbol{v}}}_{ir}=\bar{\boldsymbol{v}}_{ir}-\bar{\alpha}_i$ and $\tilde{\bar{\boldsymbol{v}}}_{id}=\bar{\boldsymbol{v}}_{id}-\dot{\bar{\alpha}}_i$, the error dynamics of the PTCF can be expressed as

$$\begin{cases}\dot{\tilde{\bar{\boldsymbol{v}}}}_{ir}=-k_{p1}\mu_2(t)\tilde{\bar{\boldsymbol{v}}}_{ir}-\dot{\mu}_2(t)\mu_2^{-1}(t)\tilde{\bar{\boldsymbol{v}}}_{ir}+\tilde{\bar{\boldsymbol{v}}}_{id}\\ \dot{\tilde{\bar{\boldsymbol{v}}}}_{id}=-k_{p2}\mu_2^2(t)\tilde{\bar{\boldsymbol{v}}}_{ir}-\ddot{\bar{\alpha}}_i\end{cases} \tag{68}$$

To accelerate the convergence of the filter error, a variable substitution is performed $\tilde{\bar{\boldsymbol{v}}}_{ik}=\mu_2(t)\tilde{\bar{\boldsymbol{v}}}_{ir}$.

From $\tilde{\bar{\boldsymbol{v}}}_{ik}$ and Equation (68), $\dot{\tilde{\bar{\boldsymbol{v}}}}_{ik}$ is rewritten as

$$\begin{aligned}\dot{\tilde{\bar{\boldsymbol{v}}}}_{ik}=&\dot{\mu}_2(t)\mu_2^{-1}(t)\tilde{\bar{\boldsymbol{v}}}_{ik}+\\ &\mu_2(t)\left(-k_{p1}\mu_2(t)\tilde{\bar{\boldsymbol{v}}}_{ir}-\dot{\mu}_2(t)\mu_2^{-1}(t)\tilde{\bar{\boldsymbol{v}}}_{ir}+\tilde{\bar{\boldsymbol{v}}}_{id}\right)=\\ &-k_{p1}\mu_2(t)\tilde{\bar{\boldsymbol{v}}}_{ik}+\mu_2(t)\tilde{\bar{\boldsymbol{v}}}_{id}\end{aligned} \tag{69}$$

From Equations (68) and (69), we have

$$\dot{\tilde{\bar{\boldsymbol{v}}}}_i=\mu_2(t)\boldsymbol{K}\tilde{\bar{\boldsymbol{v}}}_i+\boldsymbol{\chi}_i \tag{70}$$

where $\tilde{\bar{\boldsymbol{v}}}_i=\left[\tilde{\bar{\boldsymbol{v}}}_{ik}^{\mathrm{T}},\tilde{\bar{\boldsymbol{v}}}_{id}^{\mathrm{T}}\right]^{\mathrm{T}}$ and $\boldsymbol{\chi}_i=[0,-\ddot{\bar{\alpha}}_i]^{\mathrm{T}}$. The appropriate parameters are selected such that the eigenvalues of $\boldsymbol{K}=\begin{bmatrix}-k_{p1}&1\\-k_{p2}&0\end{bmatrix}$ are all negative. According to Lemma 3, a symmetric positive-definite matrix $\boldsymbol{P}\in\boldsymbol{R}^{2\times2}$ that satisfies $\boldsymbol{K}^{\mathrm{T}}\boldsymbol{P}+\boldsymbol{P}\boldsymbol{K}^{\mathrm{T}}=-\boldsymbol{Q}$ exists.

Theorem 3 For the virtual control signal $\bar{\alpha}_i$ and its derivative $\dot{\bar{\alpha}}_i$, the filter error $\tilde{\bar{\boldsymbol{v}}}_i$ can be guaranteed to converge stably to a smaller neighborhood of the origin at the prescribed time T_2 by using Equation (67) when the selection of k_{p1} and k_{p2} satisfies $k_{p1}^2>5k_{p2}$ and the eigenvalues of $\boldsymbol{P}$ and $\boldsymbol{Q}$ meet the condition $\lambda_{\max}(\boldsymbol{P})>\lambda_{\min}(\boldsymbol{P})\lambda_{\min}(\boldsymbol{Q})$.

Proof

To prove the prescribed-time stability of $\tilde{\bar{\boldsymbol{v}}}_i$, the Lyapunov function $\boldsymbol{V}_3$ is designed as

$$\boldsymbol{V}_3=\tilde{\bar{\boldsymbol{v}}}_i^{\mathrm{T}}\boldsymbol{P}\tilde{\bar{\boldsymbol{v}}}_i \tag{71}$$

From Equations (70) and (71), $\dot{\boldsymbol{V}}_3$ is rewritten as

$$\begin{aligned}\dot{\boldsymbol{V}}_3=&\dot{\tilde{\bar{\boldsymbol{v}}}}_i^{\mathrm{T}}\boldsymbol{P}\tilde{\bar{\boldsymbol{v}}}_i+\tilde{\bar{\boldsymbol{v}}}_i^{\mathrm{T}}\boldsymbol{P}\dot{\tilde{\bar{\boldsymbol{v}}}}_i=\\ &\left(\mu_2(t)\tilde{\bar{\boldsymbol{v}}}_i^{\mathrm{T}}\boldsymbol{K}^{\mathrm{T}}+\boldsymbol{\chi}_i^{\mathrm{T}}\right)\boldsymbol{P}\tilde{\bar{\boldsymbol{v}}}_i+\tilde{\bar{\boldsymbol{v}}}_i^{\mathrm{T}}\boldsymbol{P}\left(\mu_2(t)\boldsymbol{K}\tilde{\bar{\boldsymbol{v}}}_i+\boldsymbol{\chi}_i\right)\leqslant\\ &\mu_2(t)\tilde{\bar{\boldsymbol{v}}}_i^{\mathrm{T}}\left(\boldsymbol{K}^{\mathrm{T}}\boldsymbol{P}+\boldsymbol{P}\boldsymbol{K}\right)\tilde{\bar{\boldsymbol{v}}}_i+2\left\|\boldsymbol{\chi}_i^{\mathrm{T}}\boldsymbol{P}\right\|\left\|\tilde{\bar{\boldsymbol{v}}}_i\right\|\end{aligned} \tag{72}$$

When the selection of k_{p1} and k_{p2} satisfies $k_{p1}^2>5k_{p2}$, $\boldsymbol{K}$ is a Hurwitz matrix. According to Lemma 3 and Young's inequality, we have

$$\begin{aligned}\dot{\boldsymbol{V}}_3\leqslant&-\mu_2(t)\tilde{\bar{\boldsymbol{v}}}_i^{\mathrm{T}}\boldsymbol{Q}\tilde{\bar{\boldsymbol{v}}}_i+\left\|\tilde{\bar{\boldsymbol{v}}}_i\right\|^2+\left\|\boldsymbol{\chi}_i^{\mathrm{T}}\boldsymbol{P}\right\|^2\leqslant\\ &-\mu_2(t)\theta\boldsymbol{V}_3(t)+\varsigma\end{aligned} \tag{73}$$

where $\theta=\dfrac{\lambda_{\max}(\boldsymbol{P})-\lambda_{\min}(\boldsymbol{P})\lambda_{\min}(\boldsymbol{Q})}{\lambda_{\min}(\boldsymbol{P})\lambda_{\max}(\boldsymbol{P})}$ and $\varsigma\geqslant\left\|\boldsymbol{\chi}_i^{\mathrm{T}}\boldsymbol{P}\right\|^2$. Using Lemma 2, we have $\lim\limits_{t\to T_2^-}\boldsymbol{V}_3(t)=0$.

Especially, when $t\in\left[T_2,+\infty\right)$, we have $\mu_2(t)=1$. According to Equation (73), we have

$$\boldsymbol{V}_3(t)=\left(\boldsymbol{V}_3(T_2)-\frac{\varsigma}{\theta}\right)\mathrm{e}^{-\theta t}+\frac{\varsigma}{\theta}\leqslant\frac{\varsigma}{\theta} \tag{74}$$

From Equations (71) and (74), we can obtain

$$\left\|\tilde{\bar{\boldsymbol{v}}}_{ir}\right\|^2\leqslant\frac{\varsigma}{\theta\lambda_{\min}(\boldsymbol{P})} \tag{75}$$

Thus, $\left\|\tilde{\bar{\boldsymbol{v}}}_{ir}\right\|$ can rapidly converge to a neighborhood of the origin after T_2.

3.4 Distributed guidance protocol and control protocol

The containment error of the follower USV is defined as

$$\boldsymbol{z}_{1i}=\bar{\boldsymbol{R}}_i^{\mathrm{T}}(\boldsymbol{\psi}_i)\left(\bar{\boldsymbol{\eta}}_i-\boldsymbol{C}_o\left(\bar{\boldsymbol{\eta}}_k(\boldsymbol{\theta}_k)\right)\right)\in\boldsymbol{R}^2 \tag{76}$$

where variables $\bar{\boldsymbol{R}}_i^{\mathrm{T}}(\boldsymbol{\psi}_i)=\begin{bmatrix}\cos\psi_i&-\sin\psi_i\\\sin\psi_i&\cos\psi_i\end{bmatrix}$, $\bar{\boldsymbol{\eta}}_i=[x_i,y_i]^{\mathrm{T}}$ and $\bar{\boldsymbol{\eta}}_k=[x_k,y_k]^{\mathrm{T}}$.

According to Equation (14), we have $(\boldsymbol{L}_1^{-1}\boldsymbol{L}_2\otimes\boldsymbol{I}_2)\bar{\boldsymbol{\eta}}_k=(\boldsymbol{L}_1\otimes\boldsymbol{I}_2)^{-1}\tilde{\boldsymbol{\eta}}-\tilde{\boldsymbol{\eta}}$. Then, we can obtain

$$\left[(\boldsymbol{L}_1^{-1}\boldsymbol{L}_2\otimes\boldsymbol{I}_2)\bar{\boldsymbol{\eta}}_k\right]_i=-\boldsymbol{C}_o\left(\bar{\boldsymbol{\eta}}_k(\boldsymbol{\theta}_k)\right)=\left[(\boldsymbol{L}_1\otimes\boldsymbol{I}_2)^{-1}\tilde{\boldsymbol{\eta}}\right]_i-\hat{\boldsymbol{\eta}}_i \tag{77}$$

where $\left[(\boldsymbol{L}_1^{-1}\boldsymbol{L}_2\otimes\boldsymbol{I}_2)\bar{\boldsymbol{\eta}}_k\right]_{2i}\in\boldsymbol{R}^{2*1}$ represents the desired trajectory for the i-th follower. From Equations (76) and (77), we can obtain

$$\boldsymbol{z}_{1i}=\bar{\boldsymbol{R}}_i^{\mathrm{T}}(\boldsymbol{\psi}_i)\left\{\bar{\boldsymbol{\eta}}_i-\hat{\boldsymbol{\eta}}_i+\left[(\boldsymbol{L}_1\otimes\boldsymbol{I}_2)^{-1}\tilde{\boldsymbol{\eta}}\right]_{2i}\right\} \tag{78}$$

Similar to Gu et al. (2019), who addressed the underactuated issue of USVs, a small variable $\bar{\boldsymbol{z}}_{1i}=\boldsymbol{z}_{1i}+\boldsymbol{\chi}$ is introduced, where $\boldsymbol{\chi}=[\chi_0,0]^{\mathrm{T}}$. Notably, χ_0 is an auxiliary small variable to solve the underactuated issue in the sway direction.

By taking the derivative of Equation (78) and substituting Equation (2), we have

$$\begin{aligned}\dot{\bar{z}}_{1i} = \dot{z}_{1i} = & -r_i S z_{1i} + \bar{R}_i^{\mathrm{T}}(\psi_i)\left(\dot{\bar{\eta}}_i - \dot{\hat{\eta}}_i\right) + \\ & \bar{R}_i^{\mathrm{T}}(\psi_i)\left[(L_1 \otimes I_2)^{-1}\dot{\bar{\eta}}\right]_i = \\ & -r_i S(\bar{z}_{1i} - \chi) + \bar{R}_i^{\mathrm{T}}(\psi_i)\left(\dot{\bar{\eta}}_i - \dot{\hat{\eta}}_i\right) + \\ & \bar{R}_i^{\mathrm{T}}(\psi_i)\left[(L_1 \otimes I_2)^{-1}\dot{\bar{\eta}}\right]_i = \\ & -r_i S\bar{z}_{1i} + G_i\left(\bar{v}_i - \bar{\alpha}_i\right) + G_i\bar{\alpha}_i - \bar{R}_i^{\mathrm{T}}(\psi_i)\dot{\hat{\eta}}_i + \\ & \bar{R}_i^{\mathrm{T}}(\psi_i)\left[(L_1 \otimes I_2)^{-1}\dot{\bar{\eta}}\right]_i + \bar{\varpi}_i\end{aligned} \tag{79}$$

where $G_i = \begin{bmatrix} 1 & 0 \\ 0 & \chi_0 \end{bmatrix}$, $\bar{v}_i = \left[u_i, r_i\right]^{\mathrm{T}}$, and $\bar{\varpi}_i = \left[0, v_i\right]^{\mathrm{T}}$.

Given that the system velocity is observed by PTESO, combining Equation (46) yields

$$\begin{cases} \bar{v}_i = \bar{\hat{x}}_{2i} + \bar{e}_{2i} \\ \bar{\varpi}_i = \hat{x}_{2iv} + e_{iv} \end{cases} \tag{80}$$

where $\bar{\hat{x}}_{2i} = \left[\hat{u}_i, \hat{r}_i\right]^{\mathrm{T}}$, $\hat{x}_{2iv} = \left[0, \hat{v}_i\right]^{\mathrm{T}}$, $\bar{e}_{2i} = \left[\tilde{u}_i, \tilde{r}_i\right]^{\mathrm{T}}$, and $e_{iv} = \left[0, \tilde{v}_i\right]^{\mathrm{T}}$.

From Equations (80) and (79), we have

$$\begin{aligned}\dot{\bar{z}}_{1i} = & -r_i S\bar{z}_{1i} + G_i\left(\bar{\hat{x}}_{2i} - \bar{v}_{ir} + \tilde{\bar{v}}_{ir} + \bar{e}_{2i}\right) + G_i\bar{\alpha}_i - \\ & \bar{R}_i^{\mathrm{T}}(\psi_i)\dot{\hat{\eta}}_i + \bar{R}_i^{\mathrm{T}}(\psi_i)\left[(L_1 \otimes I_2)^{-1}\dot{\bar{\eta}}\right]_i + \hat{x}_{2iv} + e_{iv}\end{aligned} \tag{81}$$

The error variable is defined as

$$\bar{z}_{2i} = \bar{\hat{x}}_{2i} - \bar{v}_{ir} \tag{82}$$

From Equation (45), $\dot{\bar{z}}_{2i}$ can be derived as

$$\dot{\bar{z}}_{2i} = \dot{\bar{\hat{x}}}_{3i} + \bar{M}_i^{*-1}\mathrm{sat}(\bar{\tau}_i) + k_{1i}^2\mu_2^2(t)l_2\bar{e}_{Rx} - \dot{\bar{v}}_{ir} \tag{83}$$

where $\bar{\hat{x}}_{3i} = \left[\hat{f}_u, \hat{f}_r\right]_i^{\mathrm{T}}$, $\bar{M}_i^* = \mathrm{diag}\left\{m, I_z\right\}$, $\bar{\tau}_i = \left[\tau_u, \tau_r\right]_i^{\mathrm{T}}$, and $\bar{e}_{Rx} = \left[\left(x_i - \hat{x}_i\right)\cos\left(\psi_i\right) + \left(y_i - \hat{y}_i\right)\sin\left(\psi_i\right), \psi_i - \hat{\psi}_i\right]^{\mathrm{T}}$.

By combining Equations (81) and (83), we have

$$\begin{cases} \dot{\bar{z}}_{1i} = -r_i S\bar{z}_{1i} + G_i\bar{z}_{2i} + G_i\left(\tilde{\bar{v}}_{ir} + \bar{e}_{2i}\right) + G_i\bar{\alpha}_i - \\ \qquad \bar{R}_i^{\mathrm{T}}(\psi_i)\dot{\hat{\eta}}_i + \hat{x}_{2iv} + e_{iv} + \bar{R}_i^{\mathrm{T}}(\psi_i)\left[(L_1 \otimes I_2)^{-1}\dot{\bar{\eta}}\right]_i \\ \dot{\bar{z}}_{2i} = \dot{\bar{\hat{x}}}_{3i} + \bar{M}_i^{*-1}\mathrm{sat}(\bar{\tau}_i) + k_{1i}^2\mu_2^2(t)l_2\bar{e}_{Rx} - \dot{\bar{v}}_{ir} \end{cases} \tag{84}$$

Similar to Qin et al. (2023), to compensate for the filtering error caused by the PTCF Equation (67), the filter compensation system is designed as follows:

$$\begin{cases} \dot{\bar{\xi}}_{1i} = -\gamma_1\mu_3(t)\bar{\xi}_{1i} + G_i\left(\tilde{\bar{v}}_{ir} + \bar{\xi}_{2i}\right) - \dfrac{\bar{g}_i}{2}\bar{\xi}_{1i} \\ \dot{\bar{\xi}}_{2i} = -\gamma_2\mu_3(t)\bar{\xi}_{2i} - G_i\bar{\xi}_{1i} \end{cases} \tag{85}$$

where $\bar{g}_i = \lambda_{\max}(G_i)$, and $\mu_3(t)$ is

$$\mu_3(t) = \begin{cases} \left(\dfrac{T_3}{T_3 - t}\right)^a, & t < T_3 \\ 1, & t \geqslant T_3 \end{cases} \tag{86}$$

The error transformation yields

$$\begin{cases} s_{1i} = \bar{z}_{1i} - \bar{\xi}_{1i} \\ s_{2i} = \bar{z}_{2i} - \bar{\xi}_{2i} \end{cases} \tag{87}$$

Differentiating s_{1i} with respect to time and substituting Equations (84) and (85) into Equation (87) yield

$$\begin{aligned}\dot{s}_{1i} = & -r_i S\bar{z}_{1i} + G_i\bar{z}_{2i} + G_i\left(\tilde{\bar{v}}_{ir} + \bar{e}_{2i}\right) + G_i\bar{\alpha}_i - \\ & \bar{R}_i^{\mathrm{T}}(\psi_i)\dot{\hat{\eta}}_i - G_i\left(\tilde{\bar{v}}_{ir} + \bar{\xi}_{2i}\right) + \bar{R}_i^{\mathrm{T}}(\psi_i)\left[(L_1 \otimes I_2)^{-1}\dot{\bar{\eta}}\right]_i + \\ & \hat{x}_{2iv} + e_{iv} + \gamma_1\mu_3(t)\bar{\xi}_{1i} + \frac{\bar{g}_i}{2}\bar{\xi}_{1i} = \\ & -r_i S\bar{z}_{1i} + G_i s_{2i} + G_i\bar{\alpha}_i + G_i\bar{e}_{2i} - \\ & \bar{R}_i^{\mathrm{T}}(\psi_i)\dot{\hat{\eta}}_i + \bar{R}_i^{\mathrm{T}}(\psi_i)\left[(L_1 \otimes I_2)^{-1}\dot{\bar{\eta}}\right]_i + \\ & e_{iv} + \hat{x}_{2iv} + \gamma_1\mu_3(t)\bar{\xi}_{1i} + \frac{\bar{g}_i}{2}\bar{\xi}_{1i}\end{aligned} \tag{88}$$

The error transformation is performed again as follows:

$$\begin{cases} J_{1i} = \mu_3(t)s_{1i} \\ J_{2i} = \mu_3(t)s_{2i} \end{cases} \tag{89}$$

From Equations (88) and (89), the derivative of J_{1i} is calculated as

$$\begin{aligned}\dot{J}_{1i} = & \dot{\mu}_3(t)s_{1i} + \mu_3(t)\dot{s}_{1i} = \dot{\mu}_3(t)\mu_3^{-1}(t)J_{1i} + \\ & \mu_3(t)\left\{-r_i S\bar{z}_{1i} + G_i s_{2i} + G_i\bar{\alpha}_i + G_i\bar{e}_{2i} - \right. \\ & \bar{R}_i^{\mathrm{T}}(\psi_i)\dot{\hat{\eta}}_i + \bar{R}_i^{\mathrm{T}}(\psi_i)\left[(L_1 \otimes I_2)^{-1}\dot{\bar{\eta}}\right]_i + \\ & \left. e_{iv} + \hat{x}_{2iv} + \gamma_1\mu_3(t)\bar{\xi}_{1i} + \frac{\bar{g}_i}{2}\bar{\xi}_{1i}\right\}\end{aligned} \tag{90}$$

To stabilize J_1, the virtual control signal is constructed as follows:

$$\begin{aligned}\bar{\alpha}_i = & -G_i^{-1}\left\{\dot{\mu}_3(t)\mu_3^{-1}(t)s_{1i} + \gamma_1\mu_3(t)\bar{z}_{1i} - r_i S\bar{\xi}_{1i} - \right. \\ & \bar{R}_i^{\mathrm{T}}(\psi_i)\dot{\hat{\eta}}_i + \hat{x}_{2iv} + \bar{R}_i^{\mathrm{T}}(\psi_i)\left[(L_1 \otimes I_2)^{-1}\dot{\bar{\eta}}\right]_i + \\ & \left. \frac{\bar{g}_i}{2}\bar{\xi}_{1i} + \frac{1}{2}J_{1i}\right\}\end{aligned} \tag{91}$$

Substituting Equation (91) into Equation (90) yields

$$\dot{\boldsymbol{J}}_{1i} = -\gamma_1\mu_3(t)\boldsymbol{J}_{1i} - \boldsymbol{r}_i\boldsymbol{S}\boldsymbol{J}_{1i} + \boldsymbol{G}_i\boldsymbol{J}_{2i} - \frac{1}{2}\mu_3(t)\boldsymbol{J}_{1i} + \mu_3(t)\boldsymbol{G}_i\bar{\boldsymbol{e}}_{2i} + \mu_3(t)\boldsymbol{e}_{iv} \tag{92}$$

From Equations (84) and (85), the derivative of $\boldsymbol{s}_{2i}$ is calculated as

$$\dot{\boldsymbol{s}}_{2i} = \dot{\bar{\boldsymbol{z}}}_{2i} - \dot{\bar{\boldsymbol{\xi}}}_{2i} = \bar{\hat{\boldsymbol{x}}}_{3i} + \bar{\boldsymbol{M}}_i^{*-1}\bar{\tau}_i + \bar{\boldsymbol{M}}_i^{*-1}\Delta\bar{\tau}_i + k_{1i}^2\mu_2^2(t)l_2\bar{\boldsymbol{e}}_{Rx} - \dot{\bar{\boldsymbol{v}}}_{ir} + \gamma_2\mu_3(t)\boldsymbol{\xi}_{2i} + \boldsymbol{G}_i\boldsymbol{\xi}_{1i} \tag{93}$$

Similar to Sadek et al. (2023), to avoid the unstable effect of the saturation differential on the controlled system, the following prescribed-time anti-saturation auxiliary system is introduced:

$$\dot{\boldsymbol{q}}_i = \begin{cases} -\dfrac{\left|\boldsymbol{J}_{2i}^{\mathrm{T}}\mu_3(t)\bar{\boldsymbol{M}}_i^{*-1}\Delta\tau_i\right| + \frac{1}{2}\left\|\Delta\tau_i\right\|^2}{\left\|\boldsymbol{q}_i\right\|^2}\boldsymbol{q}_i - \\ \quad k_q\mu_3(t)\boldsymbol{q}_i - \mu_3(t)^{\frac{1}{2}}\Delta\tau_i, & \left\|\boldsymbol{q}_i\right\| \geqslant \boldsymbol{q}_0 \\ 0, & \left\|\boldsymbol{q}_i\right\| < \boldsymbol{q}_0 \end{cases} \tag{94}$$

where the boundary parameter $\boldsymbol{q}_0$ is a suitable positive constant.

The derivative of $\boldsymbol{J}_{2i}$ is

$$\dot{\boldsymbol{J}}_{2i} = \dot{\mu}_3(t)\boldsymbol{s}_{2i} + \mu_3(t)\dot{\boldsymbol{s}}_{2i} = \dot{\mu}_3(t)\mu_3^{-1}(t)\boldsymbol{J}_{2i} + \mu_3(t)\left(\bar{\hat{\boldsymbol{x}}}_{3i} + \bar{\boldsymbol{M}}_i^{*-1}\bar{\tau}_i + k_{1i}^2\mu_2^2(t)l_2\bar{\boldsymbol{e}}_{Rx} - \dot{\bar{\boldsymbol{v}}}_{ir} + \gamma_2\mu_3(t)\boldsymbol{\xi}_{2i} + \boldsymbol{G}_i\boldsymbol{\xi}_{1i} + \bar{\boldsymbol{M}}_i^{*-1}\Delta\bar{\tau}_i\right) \tag{95}$$

To stabilize $\boldsymbol{J}_2$, the following dynamic control protocol is constructed:

$$\bar{\tau}_i = -\bar{\boldsymbol{M}}_i^{*}\left[\dot{\mu}_3(t)\mu_3^{-1}(t)\boldsymbol{s}_{2i} + \bar{\hat{\boldsymbol{x}}}_{3i} + k_{1i}^2\mu_2^2(t)l_2\bar{\boldsymbol{e}}_{Rx} - \dot{\bar{\boldsymbol{v}}}_{ir} + \gamma_2\mu_3(t)\bar{\boldsymbol{z}}_{2i} + \boldsymbol{G}_i\bar{\boldsymbol{z}}_{1i} + \gamma_3\boldsymbol{q}_i + \frac{1}{2}\gamma_3\boldsymbol{J}_{2i}\right] \tag{96}$$

By substituting Equation (96), we have

$$\dot{\boldsymbol{J}}_{2i} = -\gamma_2\mu_3(t)\boldsymbol{J}_{2i} - \boldsymbol{G}_i\boldsymbol{J}_{1i} - \frac{1}{2}\gamma_3\mu_3(t)\boldsymbol{J}_{2i} - \gamma_3\mu_3(t)\boldsymbol{q}_i + \mu_3(t)\bar{\boldsymbol{M}}_i^{*-1}\Delta\bar{\tau}_i \tag{97}$$

Theorem 4 Under Assumptions 2, 3, and 4, a group of agents is considered, as described in Equation (2). The effect of the adaptive observer Equation (12), the PTESO Equation (45), the PTCF Equation (67), the filter compensation system Equation (85), the virtual control signal Equation (91), the prescribed-time anti-saturation auxiliary system (94), and the kinetic control protocol Equation (96) are also considered. Given $\gamma_1 > 0$, $\gamma_2 > 1$, $\gamma_3 > 0$, $k_q > \gamma_3 + 1$ and $a \geqslant 3$, the system guarantees that the containment error converges to a small neighborhood of the origin at the prescribed time T_3. In addition, the full-state constraints of the containment errors are implemented, which indicates that the position, velocity, and acceleration errors of the followers can converge to zero as time approaches T_3.

3.5 Stability analysis

A Lyapunov function is constructed as follows:

$$\boldsymbol{V}_{J_1} = \frac{1}{2}\boldsymbol{J}_{1i}^{\mathrm{T}}\boldsymbol{J}_{1i} \tag{98}$$

The abovementioned equation is differentiated. Considering $\boldsymbol{J}_{1i}^{\mathrm{T}}\boldsymbol{r}_i\boldsymbol{S}\boldsymbol{J}_{1i} = 0$ and substituting Equation (92) yield

$$\begin{aligned}\dot{\boldsymbol{V}}_{J_1} = {} & \boldsymbol{J}_{1i}^{\mathrm{T}}\left(-\gamma_1\mu_3(t)\boldsymbol{J}_{1i} - \boldsymbol{r}_i\boldsymbol{S}\boldsymbol{J}_{1i} + \boldsymbol{G}_i\boldsymbol{J}_{2i} - \frac{1}{2}\mu_3(t)\boldsymbol{J}_{1i} + \mu_3(t)\boldsymbol{G}_i\bar{\boldsymbol{e}}_{2i} + \mu_3(t)\boldsymbol{e}_{iv}\right) \leqslant \\ & -\gamma_1\mu_3(t)\boldsymbol{J}_{1i}^{\mathrm{T}}\boldsymbol{J}_{1i} + \boldsymbol{J}_{1i}^{\mathrm{T}}G_i\boldsymbol{J}_{2i} - \frac{1}{2}\mu_3(t)\boldsymbol{J}_{1i}^{\mathrm{T}}\boldsymbol{J}_{1i} + \\ & \mu_3(t)\left\|\boldsymbol{J}_{1i}\right\|\left(\left\|\boldsymbol{G}_i\bar{\boldsymbol{e}}_{2i}\right\| + \left\|\boldsymbol{e}_{iv}\right\|\right)\end{aligned} \tag{99}$$

According to Young's inequality, we have

$$\mu_3(t)\left\|\boldsymbol{J}_{1i}\right\|\left(\left\|\boldsymbol{G}_i\bar{\boldsymbol{e}}_{2i}\right\| + \left\|\boldsymbol{e}_{iv}\right\|\right) \leqslant \frac{1}{2}\mu_3(t)\left\|\boldsymbol{J}_{1i}\right\|^2 + \frac{1}{2}\mu_3(t)\left(\left\|\boldsymbol{G}_i\bar{\boldsymbol{e}}_{2i}\right\| + \left\|\boldsymbol{e}_{iv}\right\|\right)^2 \tag{100}$$

Substituting Equation (100) into Equation (99) yields

$$\dot{\boldsymbol{V}}_{J_1} \leqslant -\gamma_1\mu_3(t)\boldsymbol{V}_{J_1} + \boldsymbol{J}_{1i}^{\mathrm{T}}\boldsymbol{G}_i\boldsymbol{J}_{2i} + \frac{1}{2}\mu_3(t)\left(\left\|\boldsymbol{G}_i\bar{\boldsymbol{e}}_{2i}\right\| + \left\|\boldsymbol{e}_{iv}\right\|\right)^2 \tag{101}$$

Another Lyapunov function is constructed as follows:

$$\boldsymbol{V}_{J_2} = \frac{1}{2}\boldsymbol{J}_{2i}^{\mathrm{T}}\boldsymbol{J}_{2i} \tag{102}$$

By differentiating the abovementioned equation and substituting Equation (97), we obtain

$$\begin{aligned}\dot{\boldsymbol{V}}_{J_2} = {} & \boldsymbol{J}_{2i}^{\mathrm{T}}\left(-\gamma_2\mu_3(t)\boldsymbol{J}_{2i} - \boldsymbol{G}_i\boldsymbol{J}_{1i} - \frac{1}{2}\gamma_3\mu_3(t)\boldsymbol{J}_{2i} - \gamma_3\mu_3(t)\boldsymbol{q}_i + \mu_3(t)\bar{\boldsymbol{M}}_i^{*-1}\Delta\bar{\tau}_i\right) \leqslant \\ & -\gamma_2\mu_3(t)\boldsymbol{V}_{J_2} - \boldsymbol{J}_2^{\mathrm{T}}\boldsymbol{G}_i\boldsymbol{J}_{1i} - \frac{1}{2}\gamma_3\mu_3(t)\boldsymbol{J}_{2i}^{\mathrm{T}}\boldsymbol{J}_{2i} - \\ & \gamma_3\mu_3(t)\boldsymbol{J}_{2i}^{\mathrm{T}}\boldsymbol{q}_i + \mu_3(t)\boldsymbol{J}_{2i}^{\mathrm{T}}\bar{\boldsymbol{M}}_i^{*-1}\Delta\bar{\tau}_i\end{aligned} \tag{103}$$

According to Young's inequality, we have

$$-\gamma_3\mu_3(t)\boldsymbol{J}_{2i}^{\mathrm{T}}\boldsymbol{q}_i \leqslant \gamma_3\mu_3(t)\frac{1}{2}\left(\left\|\boldsymbol{J}_{2i}\right\|^2 + \left\|\boldsymbol{q}_i\right\|^2\right) \tag{104}$$

Substituting Equation (104) into Equation (103) yields

$$\dot{\boldsymbol{V}}_{J_2} \leqslant -\gamma_2\mu_3(t)\boldsymbol{V}_{J_2} - \boldsymbol{J}_{2i}^{\mathrm{T}}\boldsymbol{G}_i\boldsymbol{J}_{1i} + \frac{1}{2}\gamma_3\mu_3(t)\left\|\boldsymbol{q}_i\right\|^2 + \mu_3(t)\boldsymbol{J}_{2i}^{\mathrm{T}}\bar{\boldsymbol{M}}_i^{*-1}\Delta\bar{\tau}_i \tag{105}$$

Similarly, a Lyapunov function is constructed as follows:

$$\boldsymbol{V}_{\xi} = \frac{1}{2}\boldsymbol{\xi}_{1i}^{\mathrm{T}}\boldsymbol{\xi}_{1i} + \frac{1}{2}\boldsymbol{\xi}_{2i}^{\mathrm{T}}\boldsymbol{\xi}_{2i} \tag{106}$$

Differentiating the abovementioned equation and substituting Equation (85) yield

$$\begin{aligned}\dot{\boldsymbol{V}}_{\xi} = {}& \boldsymbol{\xi}_{1i}^{\mathrm{T}}\left(-\gamma_1\mu_3(t)\boldsymbol{\xi}_{1i} + \boldsymbol{G}_i\left(\tilde{\bar{\boldsymbol{v}}}_{ir} + \boldsymbol{\xi}_{2i}\right) - \frac{\bar{\boldsymbol{g}}_i}{2}\boldsymbol{\xi}_{1i}\right) + \\ & \boldsymbol{\xi}_{2i}^{\mathrm{T}}\left(-\gamma_2\mu_3(t)\boldsymbol{\xi}_{2i} - \boldsymbol{G}_i\boldsymbol{\xi}_{1i}\right) \leqslant \\ & -\gamma_{\min}\mu_3(t)\boldsymbol{V}_{\xi}(t) + \frac{\bar{\boldsymbol{g}}_i}{2}\left\|\tilde{\bar{\boldsymbol{v}}}_{ir}\right\|^2\end{aligned} \tag{107}$$

When $t \in [0, T_3)$, we can obtain from Lemma 2 that

$$\lim_{t \to T_3^-} \boldsymbol{V}_{\xi}(t) = 0 \tag{108}$$

When $t \in [T_3, +\infty)$, we have

$$\dot{\boldsymbol{V}}_{\xi}(t) \leqslant -\gamma_{\min}\boldsymbol{V}_{\xi}(t) + \frac{\bar{\boldsymbol{g}}_i}{2}\left\|\tilde{\bar{\boldsymbol{v}}}_{ir}\right\|^2 \tag{109}$$

Integration yields

$$\left\|\boldsymbol{\xi}_{1i}\right\| \leqslant \sqrt{\frac{\bar{\boldsymbol{g}}_i}{\gamma_{\min}}}\left\|\tilde{\bar{\boldsymbol{v}}}_{ir}\right\| \tag{110}$$

To demonstrate the stability of Equation (94), a Lyapunov function is constructed as follows:

$$\boldsymbol{V}_q = \frac{1}{2}\boldsymbol{q}_i^{\mathrm{T}}\boldsymbol{q}_i \tag{111}$$

Step 1: When $\left\|\boldsymbol{q}_i\right\| \geqslant \boldsymbol{q}_0$, differentiating the abovementioned equation and substituting Equation (94) yield

$$\begin{aligned}\dot{\boldsymbol{V}}_q = {}& \boldsymbol{q}_i^{\mathrm{T}}\left(-k_q\mu_3(t)\boldsymbol{q}_i - \frac{\left|\boldsymbol{J}_{2i}^{\mathrm{T}}\mu_3(t)\bar{\boldsymbol{M}}_i^{*-1}\Delta\tau_i\right| + \frac{1}{2}\left\|\Delta\tau_i\right\|^2}{\left\|\boldsymbol{q}_i\right\|^2}\boldsymbol{q}_i - \right. \\ & \left.\mu_3(t)^{\frac{1}{2}}\Delta\tau_i\right) \leqslant -k_q\mu_3(t)\boldsymbol{q}_i^{\mathrm{T}}\boldsymbol{q}_i - \left|\boldsymbol{J}_{2i}^{\mathrm{T}}\mu_3(t)\bar{\boldsymbol{M}}_i^{*-1}\Delta\bar{\tau}_i\right| + \\ & \frac{1}{2}\mu_3(t)\left\|\boldsymbol{q}_i\right\|^2\end{aligned} \tag{112}$$

Then, we define the entire Lyapunov function $\boldsymbol{V}_J = \boldsymbol{V}_{J_1} + \boldsymbol{V}_{J_2} + \boldsymbol{V}_{\xi} + \boldsymbol{V}_q$ and differentiate $\boldsymbol{V}_J$ to obtain

$$\begin{aligned}\dot{\boldsymbol{V}}_J \leqslant {}& -\gamma_1\mu_3(t)\boldsymbol{V}_{J_1} + \boldsymbol{J}_{1i}^{\mathrm{T}}\boldsymbol{G}_i\boldsymbol{J}_{2i} + \frac{1}{2}\mu_3(t)\left(\left\|\boldsymbol{G}_i\bar{\boldsymbol{e}}_{2i}\right\| + \left\|\boldsymbol{e}_{iv}\right\|\right)^2 - \\ & \gamma_2\mu_3(t)\boldsymbol{V}_{J_2} - \boldsymbol{J}_{2i}^{\mathrm{T}}\boldsymbol{G}_i\boldsymbol{J}_{1i} + \frac{1}{2}\gamma_3\mu_3(t)\left\|\boldsymbol{q}_i\right\|^2 + \\ & \mu_3(t)\boldsymbol{J}_{2i}^{\mathrm{T}}\bar{\boldsymbol{M}}_i^{*-1}\Delta\bar{\tau}_i - \gamma_1\mu_3(t)\left\|\boldsymbol{\xi}_{1i}\right\|^2 - \\ & \gamma_2\mu_3(t)\left\|\boldsymbol{\xi}_{2i}\right\|^2 + \frac{\bar{\boldsymbol{g}}_i}{2}\left\|\tilde{\bar{\boldsymbol{v}}}_{ir}\right\|^2 - k_q\mu_3(t)\boldsymbol{q}_i^{\mathrm{T}}\boldsymbol{q}_i - \\ & \left|\boldsymbol{J}_{2i}^{\mathrm{T}}\mu_3(t)\bar{\boldsymbol{M}}_i^{*-1}\Delta\bar{\tau}_i\right| + \frac{1}{2}\mu_3(t)\left\|\boldsymbol{q}_i\right\|^2 \leqslant \beta_1\mu_3(t)\boldsymbol{V}_J(t) + \\ & \frac{1}{2}\mu_3(t)\left(\left(\left\|\boldsymbol{G}_i\bar{\boldsymbol{e}}_{2i}\right\| + \left\|\boldsymbol{e}_{iv}\right\|\right)^2 + \bar{\boldsymbol{g}}_i\left\|\tilde{\bar{\boldsymbol{v}}}_{ir}\right\|^2\right)\end{aligned} \tag{113}$$

where $\beta_1 = \min\left\{\gamma_1, \gamma_2, \left(k_q - \gamma_3 - 1\right)\right\}$.

Step 2: When $\left\|\boldsymbol{q}_i\right\| < \boldsymbol{q}_0$, according to Young's inequality, we have

$$\begin{cases}\dfrac{1}{2}\gamma_3\mu_3(t)\left\|\boldsymbol{q}_i\right\|^2 \leqslant -\dfrac{1}{2}\gamma_3\mu_3(t)\left\|\boldsymbol{q}_i\right\|^2 + \gamma_3\mu_3(t)\boldsymbol{q}_0^2 \\ \mu_3(t)\boldsymbol{J}_{2i}^{\mathrm{T}}\bar{\boldsymbol{M}}_i^{*-1}\Delta\bar{\tau}_i \leqslant \mu_3(t)\left(\dfrac{1}{2}\left\|\boldsymbol{J}_{2i}\right\|^2 + \dfrac{1}{2}\left\|\bar{\boldsymbol{M}}_i^{-1}\Delta\bar{\tau}_i\right\|^2\right)\end{cases} \tag{114}$$

Substituting Equation (114) into Equation (105) yields

$$\begin{aligned}\dot{\boldsymbol{V}}_{J_2} \leqslant {}& -\mu_3(t)\left(\gamma_2 - 1\right)\boldsymbol{V}_{J_2} - \boldsymbol{J}_{2i}^{\mathrm{T}}\boldsymbol{G}_i\boldsymbol{J}_{1i} - \frac{1}{2}\gamma_3\mu_3(t)\left\|\boldsymbol{q}_i\right\|^2 + \\ & \gamma_3\mu_3(t)\boldsymbol{q}_0^2 + \frac{1}{2}\mu_3(t)\left\|\bar{\boldsymbol{M}}_i^{*-1}\Delta\bar{\tau}_i\right\|^2\end{aligned} \tag{115}$$

From Equation (94), we can obtain

$$\dot{\boldsymbol{V}}_q = \boldsymbol{q}_i^{\mathrm{T}}\boldsymbol{q}_i = 0 \tag{116}$$

From Equations (101), (107), (115), and (116), we can obtain

$$\begin{aligned}\dot{\boldsymbol{V}}_J \leqslant {}& -\gamma_1\mu_3(t)\boldsymbol{V}_{J_1} - \mu_3(t)\left(\gamma_2 - 1\right)\boldsymbol{V}_{J_2} - \frac{1}{2}\gamma_3\mu_3(t)\left\|\boldsymbol{q}_i\right\|^2 - \\ & \gamma_1\mu_3(t)\left\|\boldsymbol{\xi}_{1i}\right\|^2 - \gamma_2\mu_3(t)\left\|\boldsymbol{\xi}_{2i}\right\|^2 + \mu_3(t) \times \\ & \left(\frac{1}{2}\left(\left\|\boldsymbol{G}_i\bar{\boldsymbol{e}}_{2i}\right\| + \left\|\boldsymbol{e}_{iv}\right\|\right)^2 + \frac{1}{2}\left\|\bar{\boldsymbol{M}}_i^{*-1}\Delta\bar{\tau}_i\right\|^2 + \gamma_3 q_0{}^2\right)\end{aligned} \tag{117}$$

Thus, we have

$$\dot{\boldsymbol{V}}_J \leqslant -\beta_2\mu_3(t)\boldsymbol{V}_J(t) + \mu_3(t)\vartheta \tag{118}$$

where $\vartheta = \frac{1}{2}\left(\left\|\boldsymbol{G}_i\bar{\boldsymbol{e}}_{2i}\right\| + \left\|\boldsymbol{e}_{iv}\right\|\right)^2 + \frac{\bar{\boldsymbol{g}}_i}{2}\left\|\tilde{\bar{\boldsymbol{v}}}_{ir}\right\|^2 + \frac{1}{2}\left\|\bar{\boldsymbol{M}}_i^{*-1}\Delta\bar{\tau}_i\right\|^2 + \gamma_3\boldsymbol{q}_0^2$, $\beta_2 = \min\left\{\gamma_1, (\gamma_2 - 1), \gamma_2, \gamma_3\right\}$.

From inequalities (113) and (118), we can obtain

$$\dot{\boldsymbol{V}}_J \leqslant \beta_{\min}\mu_3(t)\boldsymbol{V}_J(t) + \mu_3(t)\vartheta \tag{119}$$

where $\beta_{\min} = \min\{\beta_1, \beta_2\}$.

When $t \in [0, T_3)$, integrating the abovementioned equation yields the following inequality:

$$\boldsymbol{V}_J(t) \leqslant \boldsymbol{V}_J(0)\mathrm{e}^{-\beta_{\min}\int_0^t \mu_3(s)\mathrm{d}s} + \mathrm{e}^{-\beta_{\min}\int_0^t \mu_3(s)\mathrm{d}s}\int_0^t \mu_3(t)\vartheta \mathrm{e}^{\beta_{\min}\int_0^t \mu_3(s)\mathrm{d}s}\mathrm{d}s \tag{120}$$

where $\lim_{t\to T_3^-} \boldsymbol{V}_J(t) \leqslant \frac{\vartheta}{\beta_{\min}}$. Thus, $\|\boldsymbol{J}_{1i}\|$, $\|\boldsymbol{J}_{2i}\|$, $\|\boldsymbol{\xi}_{1i}\|$, $\|\boldsymbol{\xi}_{2i}\|$, and $\|\boldsymbol{q}_i\|$ can converge to the neighborhoods $\sqrt{\frac{2\vartheta}{\beta_{\min}}}$ of the origin within the prescribed time T_3. By combining Equation (89), we can conclude that $\lim_{t\to T_3^-}\|\boldsymbol{s}_i\| \leqslant \lim_{t\to T_3^-}\mu_3^{-1}(t)\sqrt{\frac{2\vartheta}{\beta_{\min}}} = 0$. Thus, variables $\|\boldsymbol{s}_{1i}\|$ and $\|\boldsymbol{s}_{2i}\|$ converge to the origin within T_3. According to Equation (108), we have $\lim_{t\to T_3^-}\|\bar{\boldsymbol{z}}_{1i}\| = 0$. The distributed containment error of USVs can converge to 0 in T_3.

When $t \in [T_3, +\infty)$, we have

$$\dot{\boldsymbol{V}}_J \leqslant \beta_{\min}\boldsymbol{V}_J(t) + \vartheta \tag{121}$$

Integrating inequality (121) over $[0, t]$ yields

$$\boldsymbol{V}_J(t) \leqslant \left(\boldsymbol{V}_J(T_3) - \frac{\vartheta}{\beta_{\min}}\right)\mathrm{e}^{-\beta_{\min}t} + \frac{\vartheta}{\beta_{\min}} \leqslant \frac{\vartheta}{\beta_{\min}} \tag{122}$$

We obtain $\|\boldsymbol{J}_{1i}\| = \|\boldsymbol{s}_{1i}\| = \|\bar{\boldsymbol{z}}_{1i} - \boldsymbol{\xi}_{1i}\| \leqslant \sqrt{\frac{2\vartheta}{\beta_{\min}}}$, which further satisfies $\|\bar{\boldsymbol{z}}_{1i}\| \leqslant \sqrt{\frac{2\vartheta}{\beta_{\min}}} + \|\boldsymbol{\xi}_{1i}\| \leqslant \sqrt{\frac{2\vartheta}{\beta_{\min}}} + \sqrt{\frac{\bar{\boldsymbol{g}}_i}{\gamma_{\min}}}\|\tilde{\bar{\boldsymbol{v}}}_{ir}\|$. Furthermore, the variable $\Delta\bar{\tau}_i$ will converge to zero after the initial saturation stage. $\left(\|\boldsymbol{G}_i\bar{\boldsymbol{e}}_{2i}\| + \|\boldsymbol{e}_{iv}\|\right)^2$, $\|\tilde{\bar{\boldsymbol{v}}}_{ir}\|^2$, and $\boldsymbol{q}_0$ are small positive constants. The tracking error can converge to a smaller neighborhood of the origin in T_3.

Based on Ye and Song (2023), the distributed containment error exhibits prescribed-time convergence. The detailed proof is presented as follows.

By taking the derivative of Equation (89) and substituting Equation (92) into it, we have

$$\begin{aligned}\lim_{t\to T_3^-}\dot{\boldsymbol{s}}_{1i} &= \lim_{t\to T_3^-}\frac{\mathrm{d}}{\mathrm{d}t}\left(\mu_3^{-1}(t)\boldsymbol{J}_{1i}\right) = \\ &\lim_{t\to T_3^-}\left(-\mu_3^{-2}(t)\dot{\mu}_3(t)\boldsymbol{J}_{1i} + \mu_3^{-1}(t)\dot{\boldsymbol{J}}_{1i}\right) = \\ &\lim_{t\to T_3^-}\left(-\mu_3^{-2}(t)\dot{\mu}_3(t)\boldsymbol{J}_{1i} - \gamma_1\boldsymbol{J}_{1i} - \frac{1}{2}\boldsymbol{J}_{1i}\right) + \\ &\lim_{t\to T_3^-}\left(-\mu_3^{-1}(t)\boldsymbol{r}_i\boldsymbol{S}\boldsymbol{J}_{1i} + \mu_3^{-1}(t)\boldsymbol{G}_i\boldsymbol{J}_{2i}\right) + \\ &\lim_{t\to T_3^-}\left(\boldsymbol{G}_i\bar{\boldsymbol{e}}_{2i} + \boldsymbol{e}_{iv}\right)\end{aligned} \tag{123}$$

Based on $\lim_{t\to T_3^-}\mu_3^{-1}(t) = 0$ and $\lim_{t\to T_3^-}\left(\boldsymbol{G}_i\bar{\boldsymbol{e}}_{2i} + \boldsymbol{e}_{iv}\right) = 0$, Equation (123) can be expressed as

$$\lim_{t\to T_3^-}\dot{\boldsymbol{s}}_{1i} = \lim_{t\to T_3^-} -\varsigma\boldsymbol{J}_{1i} \tag{124}$$

where $\varsigma = \mu_3^{-2}(t)\dot{\mu}_3(t) + \gamma_1 + \frac{1}{2}$. Given that the variable $\boldsymbol{J}_1$ is bounded when $t \to T_3^-$, a constant vector $\bar{\boldsymbol{\chi}}$ exists such that $\lim_{t\to T_3^-}\boldsymbol{J}_{1i} = \lim_{t\to T_3^-}\mu_3(t)\boldsymbol{s}_{1i} = \lim_{t\to T_3^-}\frac{{t_f}^a\boldsymbol{s}_{1i}}{\left(t_f - t\right)^a} = \bar{\boldsymbol{\chi}}$. By applying L'Hôpital's rule to the equation and substituting Equation (124) into it, we have

$$\lim_{t\to T_3^-}\boldsymbol{J}_{1i} = \lim_{t\to T_3^-}\frac{\varsigma{t_f}^a\boldsymbol{J}_{1i}}{a\left(t_f - t\right)^{a-1}} = \lim_{t\to T_3^-}\frac{\varsigma{t_f}^{2a}\boldsymbol{s}_{1i}}{a\left(t_f - t\right)^{2a-1}} = \bar{\boldsymbol{\chi}} \tag{125}$$

According to Equation (124), $\lim_{t\to T_3}\dot{\boldsymbol{s}}_1 = 0$ holds.

From $\lim_{t\to T_3^-}\dot{\boldsymbol{s}}_{1i} = \lim_{t\to T_3^-} -\varsigma\mu_3(t)\boldsymbol{s}_{1i}$ and Equation (124), we can obtain

$$\begin{aligned}\lim_{t\to T_3^-}\dot{s}_{1i} &= \lim_{t\to T_3}\frac{\varsigma{t_f}^a\dot{s}_{1i}}{a\left(t_f - t\right)^{a-1}} = \cdots = \\ &\lim_{t\to T_3^-}(-1)^{(q+1)}\varsigma{t_f}^a\frac{(a-q)!}{(a)!}\frac{\boldsymbol{s}_{1i}^{(q)}}{\left(t_f - t\right)^{a-q}} = 0\end{aligned} \tag{126}$$

Given that $\lim_{t\to T_3^-}\xi_{1i}^{(q)} = 0$, Equation (126) can be written as follows:

$$\begin{aligned}\lim_{t\to T_3^-}\bar{z}_{1i}^{(q)} &= \lim_{t\to T_3^-}s_1^{(q)} = \\ &\lim_{t\to T_3^-}\frac{(-1)^{(q+1)}}{\varsigma{t_f}^a}\frac{(a)!\left(t_f - t\right)^{a-q}}{(a-q)!}\dot{s}_1 = 0\end{aligned} \tag{127}$$

Therefore, when $a = 3 > q$, the first- and second-order derivatives of error $\bar{\boldsymbol{z}}_{1i}$ can stably converge to the origin at the prescribed time T_3. The proof of full-state convergence, including errors, is completed.

4 Numerical simulations

4.1 Parameter settings

Several simulations have been conducted to assess the efficacy of the prescribed-time distributed containment control method. A MAS consisting of multiple USVs, including five followers and two virtual leaders, is consid-

ered. The sets $V_F = \{1, 2, 3, 4, 5\}$ and $V_L = \{6, 7\}$ denote the follower and virtual leader nodes, respectively. The communication topology among agents is displayed in Figure 4.

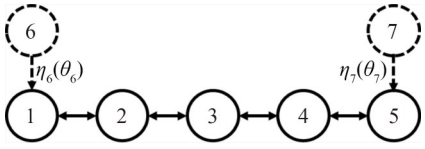


Figure 4 Communication topology

The Laplacian matrix of the entire distributed system can be represented in the form of a block matrix as follows:

$$\boldsymbol{L}_1 = \begin{bmatrix} 2 & -1 & 0 & 0 & 0 \\ -1 & 2 & -1 & 0 & 0 \\ 0 & -1 & 2 & -1 & 0 \\ 0 & 0 & -1 & 2 & -1 \\ 0 & 0 & 0 & -1 & 2 \end{bmatrix}, \boldsymbol{L}_2 = \begin{bmatrix} -1 & 0 \\ 0 & 0 \\ 0 & 0 \\ 0 & 0 \\ 0 & -1 \end{bmatrix} \tag{128}$$

Similar to that in Gu et al. (2019), the trajectory information of virtual leaders 6 and 7 can be represented as follows:

$$\begin{cases} \boldsymbol{\eta}_6(\theta_6) = \begin{bmatrix} 0.1\sqrt{2}\,\theta_6 - 6\sqrt{2}\cos\left(0.005\theta_6 + \dfrac{9\pi}{10}\right) + 20 \\ 0.1\sqrt{2}\,\theta_6 + 6\sqrt{2}\cos\left(0.005\theta_6 + \dfrac{9\pi}{10}\right) - 40 \end{bmatrix}^{\mathrm{T}} \\ \boldsymbol{\eta}_7(\theta_7) = \begin{bmatrix} 0.1\sqrt{2}\,\theta_7 + 6\sqrt{2}\cos\left(0.005\theta_7 + \dfrac{9\pi}{10}\right) - 20 \\ 0.1\sqrt{2}\,\theta_7 - 6\sqrt{2}\cos\left(0.005\theta_7 + \dfrac{9\pi}{10}\right) - 20 \end{bmatrix}^{\mathrm{T}} \end{cases} \tag{129}$$

To achieve a parallel formation of the five USVs at a unified speed, the trajectory update variable can be set as $\theta_6 = \theta_7 = v_s t$, where v_s denotes the update speed of the trajectory variable. It is used to adjust the overall speed of the USV formation.

In the simulation, the parameters of the model ship CyberShip II in Skjetne et al. (2005) (as shown in Figure 5) are used for the follower USVs in our study.

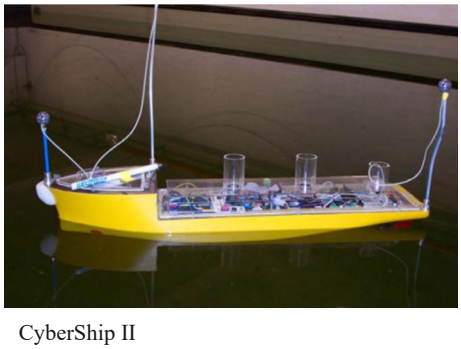


Figure 5 CyberShip II

The corresponding hydrodynamic parameters of the model are set as $m = 23.8$, $I_z = 1.76$, $x_g = 0.046$, $X_{\dot{u}} = -2.0$, $Y_{\dot{v}} = -10.0$, $Y_{\dot{r}} = 0$, $N_{\dot{v}} = 0$, $N_{\dot{r}} = -1.0$, $X_u = -0.722\,5$, $X_{uu} = -1.327\,4$, $X_{uuu} = -5.866\,4$, $Y_v = -0.861\,2$, $Y_{vv} = -36.282\,3$, $Y_{|r|v} = -0.805$, $Y_r = 0.107\,9$, $Y_{|v|r} = -0.845$, $Y_{rr} = -3.45$, $N_v = 0.105\,2$, $N_{|v|v} = 5.043\,7$, $N_{|r|v} = 0.13$, $N_r = -1.9$, $N_{|v|r} = 0.08$, and $N_{|r|r} = -0.75$.

Owing to the time-varying disturbance forces resulting from the combined effects of wind, waves, currents, and external environmental factors during sailing, these disturbances can be modeled as a sine wave superimposed on a first-order Gauss-Markov process. It can be expressed as follows:

$$\begin{cases} \tau_{iwu} = 1.2\sin(0.15t) + \tau_{du} + 2 \\ \tau_{iwv} = 0.4\sin(0.15t) + \tau_{dv} \\ \tau_{iwr} = 1.3\sin(0.15t) + \tau_{dr} \\ \dot{\tau}_{du} + b_1\tau_{du} = w_u \\ \dot{\tau}_{dv} + b_2\tau_{dv} = w_v \\ \dot{\tau}_{dr} + b_3\tau_{dr} = w_r \end{cases} \tag{130}$$

where parameters τ_{du}, τ_{dv}, and τ_{dr} are random variables generated by a first-order Gauss-Markov process, with Gaussian white noise w_u, w_v, and w_r whose mean values are 0.5 and variances are 1. b_1, b_2, and b_3 represent time constants and are set as 0.5.

The initial information and parameters of the USVs, the prescribed-time distributed position observer, the PTESO, and the PTCF are presented in Tables 2–6.

Table 2 Initial information of the USVs

USV	x	y	ψ	$\boldsymbol{v}$
1	12	−48	8	
2	3	−42	9	
3	−6	−36	9	$[0, 0, 0]^{\mathrm{T}}$
4	−16	−30	9	
5	−25	−24	9	

Table 3 Initial values and parameters for the position observer

Initial values				Parameters		
$\hat{\boldsymbol{\eta}}_i$	$\hat{\boldsymbol{v}}_i$	$\hat{\boldsymbol{a}}_i$	$\hat{\gamma}_i$	k_1	k_2	k_3
$[0, 0]^{\mathrm{T}}$	$[0, 0]^{\mathrm{T}}$	$[0, 0]^{\mathrm{T}}$	0	5	5	5

Table 4 Initial values and parameters for the PTESO

Initial values			Parameters			
$\hat{\boldsymbol{x}}_{1i}$	$\hat{\boldsymbol{x}}_{2i}$	$\hat{\boldsymbol{x}}_{3i}$	k_{1i}	l_1	l_2	l_3
$[0, 0, 0]^{\mathrm{T}}$	$[0, 0, 0]^{\mathrm{T}}$	$[0, 0, 0]^{\mathrm{T}}$	4	6	11	6

Table 5 Initial values and parameters for the command filter

Initial values		Parameters	
$\bar{\boldsymbol{v}}_{ir}(0)$	$\bar{\boldsymbol{v}}_{id}(0)$	k_{p1}	k_{p2}
$[0,0]^{\mathrm{T}}$	$[0,0]^{\mathrm{T}}$	10	5

Table 6 Initial values and parameters for the filter compensation system

Initial values		Parameters	
$\boldsymbol{\xi}_{1i}(0)$	$\boldsymbol{\xi}_{2i}(0)$	γ_1	γ_2
$[0,0]^{\mathrm{T}}$	$[0,0]^{\mathrm{T}}$	5	5

The initial values for the prescribed-time anti-saturation auxiliary system are set as $\boldsymbol{q}_i(0) = [0,0]^{\mathrm{T}}$, the parameter is $k_q = 20$, and the boundary parameter is $q_0 = 0.1$. In the kinematic virtual guidance law, the parameters are set as $\gamma_1 = 0.3$. In the dynamic control law, the parameters are set as $\gamma_2 = 5, \gamma_3 = 1$, and the saturation upper limit is set to $\tau_{\max} = 50$ N (N·m). To address the underactuated issue, the virtual variable is set to $\delta_0 = 0.3$. The initial value of the trajectory variable is set to $\theta_6 = \theta_7 = 0$, and the update speed is set to $v_s = 3$.

The prescribed time constants are set as $T_1 = 2.5$ s, $T_2 = 3$ s, and $T_3 = 12$ s. The three prescribed-time scaling functions are set as follows:

$$\begin{cases} \mu_1(t) = \begin{cases} \dfrac{2.5}{2.5 - t}, & t < 2.5 \\ 1, & t \geqslant 2.5 \end{cases} \\ \mu_2(t) = \begin{cases} \dfrac{3}{3 - t}, & t < 3 \\ 1, & t \geqslant 3 \end{cases} \\ \mu_3(t) = \begin{cases} \left(\dfrac{12}{12 - t}\right)^3, & t < 12 \\ 1, & t \geqslant 12 \end{cases} \end{cases} \tag{131}$$

4.2 Simulation results

The numerical simulations are depicted in Figures 6–20.

The USVs can track the desired convex hull spanned by the virtual leaders within $T_3 = 12$ s. They form a parallel formation and maintain the same speed, as illustrated in Figure 6. As displayed in Figures 7 and 8, under the influence of the prescribed-time distributed adaptive position observer, the observation errors of the five USVs for the desired convex hull can rapidly converge to a small neighborhood of zero within the prescribed time $T_1 = 2.5$ s. Similarly, as presented in Figures 9 and 10, under the influence of the PTESO, the observation errors of the five USVs for the general uncertainties in their longitudinal and yaw directions can rapidly converge to a small neighborhood of zero within the prescribed time $T_2 = 3$ s. As depicted in Figures 11 and 12, the observation errors of the five USVs in their longitudinal velocity and yaw angular velocity can also rapidly converge to a small neighborhood of zero within $T_2 = 3$ s. As shown in Figures 13 and 14, under the influence of the PTCF, the filtering errors in the longitudinal and transverse directions can rapidly converge to a small neighborhood of zero within $T_2 = 3$ s. Figures 15 and 16 reveal that the longitudinal and lateral containment errors of the five USVs can rapidly converge to a small neighborhood of zero within the prescribed time $T_3 = 12$ s.

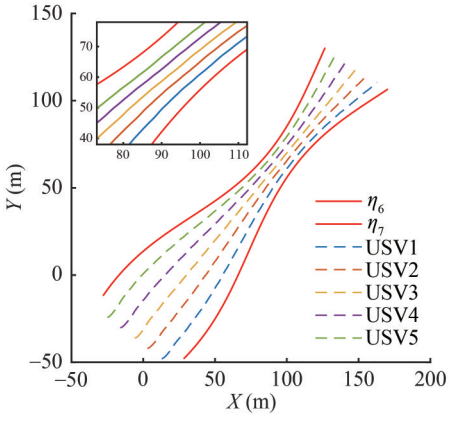


Figure 6 Distributed containment control of USVs

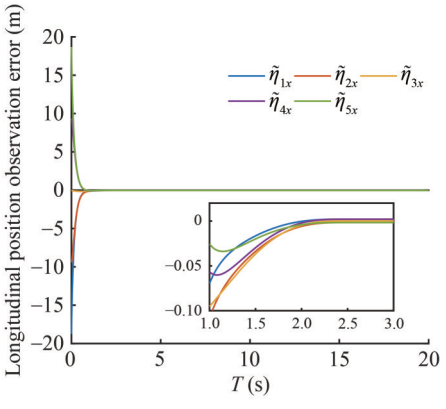


Figure 7 Longitudinal position observation errors of the position observer

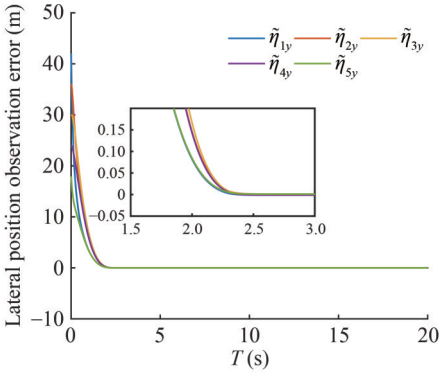


Figure 8 Lateral position observation errors of the position observer

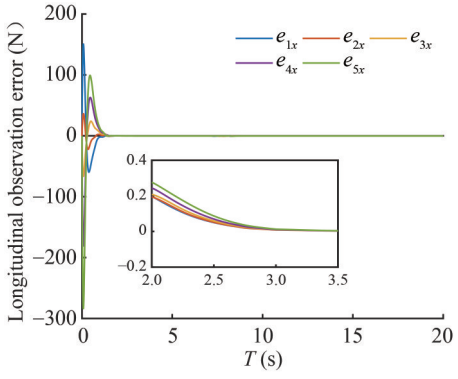


Figure 9 Observation errors of PTESO for longitudinal general uncertainties

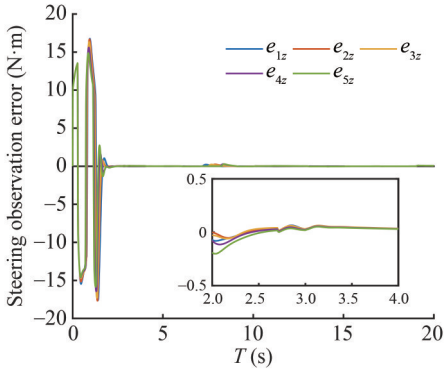


Figure 10 Observation errors of PTESO for yaw general uncertainties

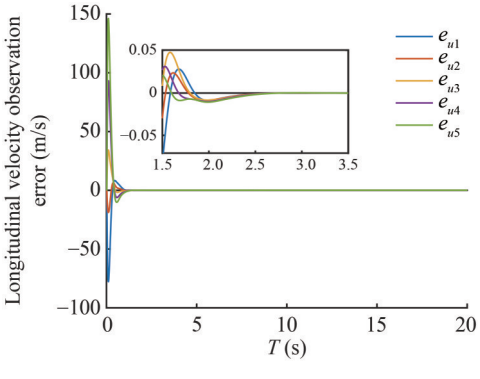


Figure 11 Observation errors of PTESO for longitudinal velocity

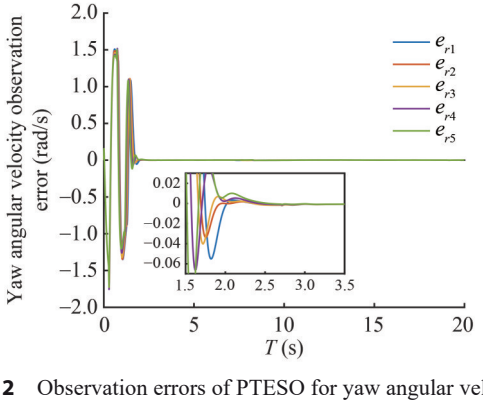


Figure 12 Observation errors of PTESO for yaw angular velocity

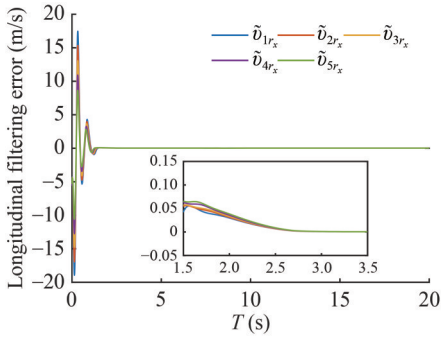


Figure 13 Filtering errors in the longitudinal directions

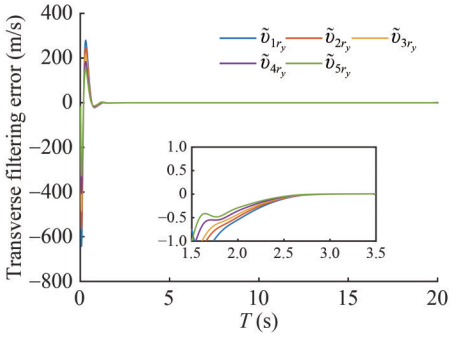


Figure 14 Filtering errors in the transverse directions

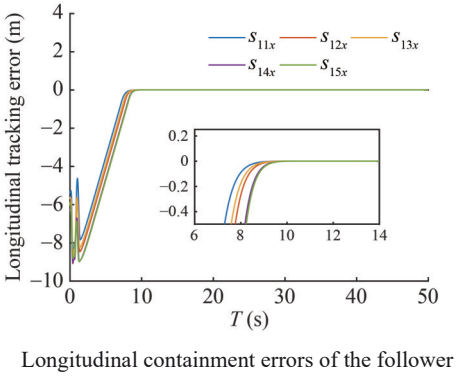


Figure 15 Longitudinal containment errors of the follower USVs

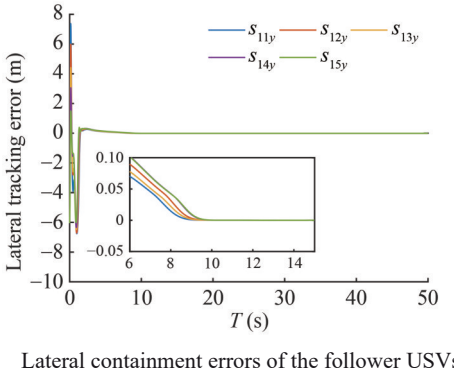


Figure 16 Lateral containment errors of the follower USVs

Figures 17 and 18 show that the longitudinal thrust and steering torque of the five USVs reach stable values within $T_3 = 12$ s. The thrust of USV varies in the range of 0–10 N, which is in line with practical engineering. As illustrated

in Figures 19 and 20, the longitudinal velocity and angular rate of the five follower USVs reach stable values within the prescribed time $T_3 = 12$ s, with a stable velocity of $u_i \approx 0.6$ m/s, $i = 1, \cdots, 5$.

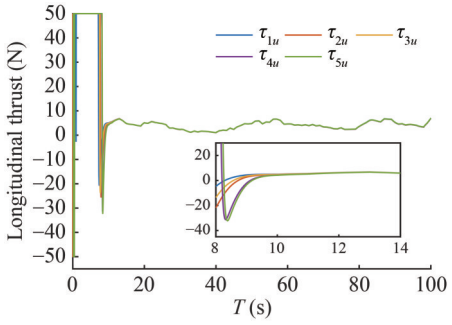


Figure 17 Longitudinal thrust of the follower USVs

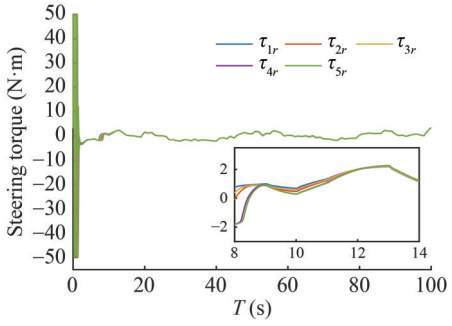


Figure 18 Steering torque of the follower USVs

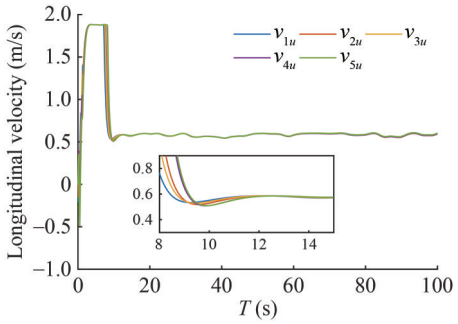


Figure 19 Longitudinal velocity of the follower USVs

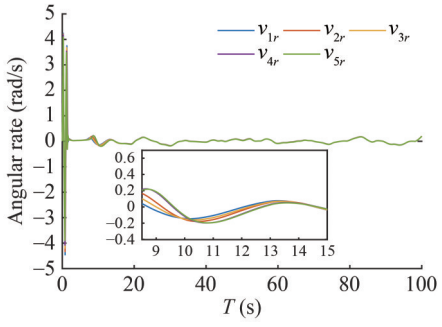


Figure 20 Angular rate of the follower USVs

Remark 2 The distributed prescribed-time containment control system for USVs has been designed. The PTESO, PTCF, and controller can operate independently on each USV. They require only neighbor information and the distributed observer to reduce the centralized computing burden. The controller, which is based on key equations, avoids computationally intensive iterative processes such as MPC and DRL. Thus, it is suitable for embedded platforms. Simulations show that the control law converges within T_3 with smooth control inputs, which suggests that the algorithm satisfies real-time control requirements.

5 Conclusions

This study presents a distributed containment control method based on a prescribed-time control for USVs to solve the complexities in distributed containment control. Initially, the desired trajectory is estimated using the prescribed-time adaptive observer. The unknown disturbance terms in the USV model are observed using the PTESO within the prescribed time. Then, a distributed prescribed-time guidance law and controllers are constructed based on a command filter and an anti-saturation auxiliary system. By employing the proposed controllers, the underactuated USVs can converge to the desired convex hull by adjusting the distances among them based on the channel width. The full-state constraints for containment error dynamics are determined. Simulation results reveal that the proposed control method can attain containment control at a prescribed time in the presence of system uncertainty, generalized disturbances, and input saturation. However, the proposed algorithm is only applicable for slow time-varying external disturbances and bounded input saturation. Considering the complexity of marine environments, the topological structure of USVs may vary, including the addition of new USVs or the failure of certain USVs. Therefore, our future research aims to extend the proposed approach by addressing the containment control of larger-scale USV systems with switching network topologies and event-triggering communication mechanisms.

Competing interest Yanchao Sun and Hongde Qin are editorial board members for the Journal of Marine Science and Application and were not involved in the editorial review, or the decision to publish this article. All authors declare that there are no other competing interest.

References

Chang L, Han QL, Ge X, Zhang C, Zhang X (2021) On designing distributed prescribed finite-time observers for strict-feedback nonlinear systems. IEEE Transactions on Cybernetics 51(9): 4695-4706. https://doi.org/10.1109/TCYB.2019.2951067

Chen C, Han Y, Zhu S, Zeng Z (2023) Distributed fixed-time tracking and containment control for second-order multi-agent systems: A nonsingular sliding-mode control approach. IEEE

Transactions on Network Science and Engineering 10(2): 687-697. https://doi.org/10.1109/TNSE.2022.3217536

Chen T, Shan J (2021) Distributed spacecraft attitude tracking and synchronization under directed graphs. Aerospace Science and Technology 109:106432. https://doi.org/10.1016/j.ast.2020.106432

Cui L, Jin N (2021) Prescribed-time ESO-based prescribed-time control and its application to partial IGC design. Nonlinear Dynamics 106(1): 491-508. https://doi.org/10.1007/s11071-021-06859-5

Fossen TI (2011) Handbook of marine craft hydrodynamics and motion control. Hoboken:Sussex/John Willy & Sons Ltd. https://doi.org/10.1002/9781119994138

Gao H, Xia Y, Zhang X, Zhang G (2022) Distributed fixed-time attitude coordinated control for multiple spacecraft with actuator saturation. Chinese Journal of Aeronautics 35(4): 292-302. https://dor.org/10.1016/j.cja.2021.05.022

Gu N, Wang D, Peng Z, Liu L (2019) Observer-based finite-time control for distributed path maneuvering of underactuated unmanned surface vehicles with collision avoidance and connectivity preservation. IEEE Transactions on Systems, Man, and Cybernetics: Systems 51(8): 5105-5115. https://doi.org/10.1109/TSMC.2019.2944521

Gu N, Wang D. Peng Z, Wang J, Han QL (2022) Advances in line-of-sight guidance for path following of autonomous marine vehicles: An overview. IEEE Transactions on Systems, Man, and Cybernetics: Systems 53(1): 12-28. https://doi.org/10.1109/TSMC.2022.3162862

Jiang C, Xiong X, Xiang X, Zeng Z, Zhang F (2025) Underwater perception and autonomous operation for underwater vehicle-manipulator systems: Methodology andexperiment. IEEE/ASME Transactions on Mechatronics (Early Access) 1-12. https://doi.org/10.1109/TMECH.2025.3563632

Jiang Y, Peng Z, Wang D, Yin Y, Han QL (2021) Cooperative target enclosing of ring-networked underactuated autonomous surface vehicles based on data-driven fuzzy predictors and extended state observers. IEEE Transactions on Fuzzy Systems 30(7): 2515-2528. https://doi.org/10.1109/TFUZZ.2021.3087920

Li J, Xiang X, Dong D, Yang S (2023) Prescribed time observer based trajectory tracking control of autonomous underwater vehicle with tracking error constraints. Ocean Engineering 274: 114018. https://doi.org/10.1016/j.oceaneng.2023.114018

Li J, Xiang X, Zhang Q, Yang S (2024) Robust practical prescribed time trajectory tracking of USV with guaranteed performance. Ocean Engineering 302: 117622. https://doi.org/10.1016/j.oceaneng.2024.117622

Li M, Guo C, Yu H (2021) Global finite-time control for coordinated path following of multiple underactuated unmanned surface vehicles along one curve under directed topologies. Ocean Engineering 237: 109608. https://doi.org/10.1016/j.oceaneng.2021.109608

Li M, Guo C, Yu H, Yuan Y (2022) Line-of-sight-based global finite-time stable path following control of unmanned surface vehicles with actuator saturation. ISA Transactions 125: 306-317. https://doi.org/10.1016/j.isatra.2021.07.009

Li X, Ren C, Ma S, Zhu X (2020) Compensated model-free adaptive tracking control scheme for autonomous underwater vehicles via extended state observer. Ocean Engineering 217: 107976. https://doi.org/10.1016/j.oceaneng.2020.107976

Liu D, Liu Z, Chen CP, Zhang Y (2021) Prescribed-time containment control with prescribed performance for uncertain nonlinear multi-agent systems. Journal of the Franklin Institute 358(3): 1782-1811. https://doi.org/10.1016/j.jfranklin.2020.12.021

Liu L, Zhang W, Wang D, Peng Z (2020) Event-triggered extended state observers design for dynamic positioning vessels subject to unknown sea loads. Ocean Engineering 209: 107242. https://doi.org/10.1016/j.oceaneng.2020.107242

Mei J, Ren W, Ma G (2012) Distributed containment control for Lagrangian networks with parametric uncertainties under a directed graph. Automatica 48(4): 653-659. https://doi.org/10.1016/j.automatica.2012.01.020

Mu D, Feng Y, Wang G, Fan Y, Zhao Y (2022) Single-parameter-learning-based robust adaptive control of dynamic positioning ships considering thruster system dynamics in the input saturation state. Nonlinear Dynamics 110(1): 395-412. https://doi.org/10.1007/s11071-022-07657-3

Peng Z, Wang J, Wang D, Han QL (2021) An overview of recent advances in coordinated control of multiple autonomous surface vehicles. IEEE Transactions on Industrial Informatics 17(2): 732-745. https://doi.org/10.1109/TII.2020.3004343

Qin H, Yang H, Sun Y, Feng L (2023) Fixed-time stable bilateral teleoperation of underwater manipulator using prescribed performance terminal sliding surfaces. Journal of the Franklin Institute 360(4): 3280-3306. https://doi.org/10.1016/j.jfranklin.2023.01.028

Sadek BA, Badreddine EH, Noreddine C, El Houssaine T (2023) Achieving prescribed-time stabilization in nonlinear TCP/AQM systems with input saturation. IEEE Transactions on Network Science and Engineering 11(1): 1363-1373. https://doi.org/10.1109/tnse.2023.3322514

Skjetne R, Fossen TI, Kokotović PV (2005) Adaptive maneuvering, with experiments, for a model ship in a marine control laboratory. Automatica 41(2): 289-298. https://doi.org/10.1016/j.automatica.2004.10.006

Slotine JJE, Li W (1991) Applied nonlinear control . Englewood Cliffs, NJ: Prentice Hall 199(1): 705

Song Y, Wang Y, Holloway J, Krstic M (2017) Time-varying feedback for regulation of normal-form nonlinear systems in prescribed finite time. Automatica 83: 243-251. https://doi.org/10.1016/j.automatica.2017.06.008

Sun Y, Liu M, Qin H, Wang H, Ding Z (2024) Full prescribed performance trajectory tracking control strategy of autonomous underwater vehicle with disturbance observer. ISA Transactions 151: 117-130. https://doi.org/10.1016/j.isatra.2024.06.002

Wang P, Zhang X, Ge SS (2021) Prescribed-time control with explicit reference governor for a class of constrained cascaded systems. International Journal of Robust and Nonlinear Control 31(13): 6422-6437. https://doi.org/10.1002/rnc.5620

Wang Z, Xiang X, Xiong X, Yang S (2025) Position-based acoustic visual servo control for docking of autonomous underwater vehicle using deep reinforcement learning. Robotics and Autonomous Systems 186: 104914. https://doi.org/10.1016/j.robot.2024.104914

Wu W, Peng Z, Wang D, Liu L, Han QL (2022) Network-based line-of-sight path tracking of underactuated unmanned surface vehicles with experiment results. IEEE Transactions on Cybernetics 52(10): 10937-10947. https://doi.org/10.1109/TCYB.2021.3074396

Wu W, Zhang Y, Zhang W, Xie W (2023) Output-feedback finite-time safety-critical coordinated control of path-guided marine surface vehicles based on neurodynamic optimization. IEEE Transactions on Systems, Man, and Cybernetics: Systems 53(3): 1788-1800. https://doi.org/10.1109/TSMC.2022.3205637

Ye H, Song Y (2023) Prescribed-time tracking control of MIMO nonlinear systems with nonvanishing uncertainties. IEEE Transactions on Automatic Control 68(6): 3664-3671. https://doi.

org/10.1109/TAC.2022.3194100

Yi S, Wang J, Li B (2017) Composite backstepping control with finite-time convergence. Optik 142: 260-272. https://doi.org/10.1016/j.ijleo.2017.05.070

Zhang J, Yu S, Wu D, Yan Y (2020) Nonsingular fixed-time terminal sliding mode trajectory tracking control for marine surface vessels with anti-disturbances. Ocean Engineering 217: 108158. https://doi.org/10.1016/j.oceaneng.2020.108158

Zhang J, Yu S, Yan Y (2019) Fixed-time output feedback trajectory tracking control of marine surface vessels subject to unknown external disturbances and uncertainties. ISA Transactions 93: 145-155. https://doi.org/10.1016/j.isatra.2019.03.007

Zhang Q, Zhang J, Chemori A, Xiang X (2018) Virtual submerged floating operational system for robotic manipulation. Complexity 2018(1): 9528313. https://doi.org/10.1155/2018/9528313

Zhang Y, Wang D, Yin Y, Peng Z (2021) Event-triggered distributed coordinated control of networked autonomous surface vehicles subject to fully unknown kinetics via concurrent-learning-based neural predictor. Ocean Engineering 234: 108966. https://doi.org/10.1016/j.oceaneng.2021.108966